ANALYZING MODAL DECOMPOSITION DATA OF FINITE ANTENNA
ARRAYS

BY

JOHN M. OUTWATER JR.

DISSERTATION

Submitted in partial fulfillment of the requirements
for the degree of Doctor of Philosophy in Electrical and Computer Engineering
in the Graduate College of the
University of Illinois at Urbana-Champaign, 2019

Urbana, Illinois

Doctoral Committee:

Professor Jennifer T. Bernhard, Chair
Professor Steven J. Franke
Professor Jian-Ming Jin
Assistant Professor Songbin Gong

ABSTRACT

Traditional antenna array theory is well suited for guiding the design of very large, uniform arrays. When an array is large enough one can often approximate that the array is of infinite extent, greatly simplifying the analysis of the structure and significantly reducing the cost of simulation. However, as array size decreases these approximations break down and the total radiating structure is subject to finite array effects. Such effects can perturb the expected radiation patterns and cause large variations in impedance across the array elements. These effects can be partially mitigated through conditioning certain elements of the array, or adding terminated "dummy" elements to the array. These methods often require many iterations of simulation and can become costly as the number of parameterized variables grows.

In order to better understand the finite array effects and reduce our dependency on parametric simulations, we study a modal decomposition of the array currents. In particular we use characteristic mode analysis (CMA) which produces an indexed set of "simpler" eigencurrents, and eigenvalues that dictate the energy storage properties of the modes. These modes are dependent entirely on the method of moments impedance matrix of the structure, and therefore are independent of the array feeding method. Whereas CM is often used in the study of single port, electrically small structures that are dominated by one or two modes, our template arrays are electrically large and made of multiple disjoint elements, with multiple feed points. This work explores and catalogs the types of characteristic mode results attained from two different classes of antenna arrays. We calculate and compare the accuracy of our modal summations and determine how matrix conditioning affects the modal decompositions of different arrays and different array elements. These results can help establish expected accuracy guidelines for this electrically large class of problems.

For Gramps—always reading, always learning.

TABLE OF CONTENTS

CHAPTER 1

INTRODUCTION

1.1 Background

Antenna arrays are used in a myriad of applications, from advanced home wireless networking to military-grade radar systems. Composed of two or more antennas, the elements are spaced and excited such that the radiated fields constructively (or destructively) interfere, enhancing (or degrading) the total gain in a desired direction. Varying the amplitude and phase of the element excitations can allow us to electronically control the orientation of our beam-pattern. This allows rapid modifications of our radiation pattern and reduces the need for mechanical means of rotating and reorienting the array platform.

Basic array analysis often treats the elements as non-interacting entities, acting as if each element were operating in free-space. This approach, while suitable for only simple applications, allows us to assume that all of the array element currents are proportional to their incident signals. Furthermore, it allows us to synthesize the total array pattern as a product of a single-element pattern and an array pattern [1]. For most practical applications one must additionally account for mutual coupling effects which cause our elements to behave differently than they would in a free-space situation. Mutual coupling in arrays can be attributed to one of three mechanisms, as illustrated in Figure 1.1. Direct space coupling occurs directly between the elements of the array, with the radiation from one perturbing the field of another. Increasing element spacing can reduce this effect, but often at the cost of introducing grating lobes to the radiation pattern. Indirect coupling occurs when radiation from the array is scattered by nearby conductive structures, such as the platform the array is mounted on. While an electrically large ground-plane can act as a reflector, an irregular ground-plane can contribute to indirect
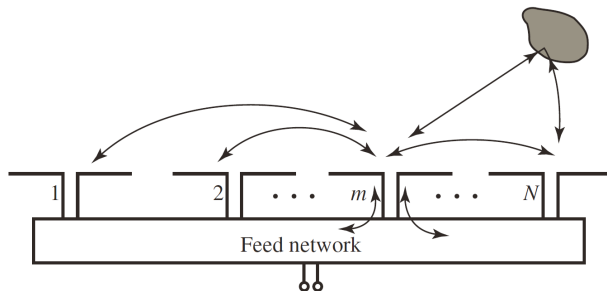
Figure 1.1: Mechanisms for coupling between elements of an array, from [1].

coupling in less predictable ways. The final mechanism is coupling through the feed structure of the array. Given the need for precise control over element excitation, feed-networks can often be the most sensitive aspect of an array design. Non-linear elements and phase-shifters can make it difficult to model an advanced feed, and therefore make it a complex task to isolate and prevent feed network coupling.

Even with these considerations in mind, most array design methodologies are best suited for guiding the design of very large, uniform arrays. When an array is large enough one can often approximate that the array is of infinite extent, greatly simplifying the analysis of the structure and significantly reducing the cost of simulation. In such cases one can assume that all of the elements have identical surroundings (in at least one dimension) and therefore are subject to identical coupling effects. However, as array size decreases these approximations break down and the total radiating structure is subject to finite array effects that can perturb the expected radiation patterns and cause large variations in impedance across the array elements [2]. These effects can be partially mitigated through conditioning certain elements of the array, or adding terminated "dummy" elements to the array. These methods often require many iterations of simulation and can become costly as the number of parameterized variables grows. Most importantly, the changes made through parametric optimization are often not generalizable. That is to say, we know they improve performance but it is often not clear what is the cause of the improvement. Without a more generalizable definition of optimization, one must perform these parametrics each time a base design is modified.

1.2 Motivation

The goal of this research is to investigate the application of characteristic mode analysis to the problem space of electrically large radiators, specifically resonant length antenna arrays. Characteristic mode theory applications are being widely explored in the contemporary literature. This reinvigorated area of research has been largely focused on the study of electrically small and resonant length antennas [3, 4, 5, 6] and CMA solvers are becoming commonplace in commercial solver suites. In recent years studies of CMA and its application to simple arrays has garnered interest [7, 8, 9]. However, we must determine specific metrics of interest relevant to the application space and determine if this particular modal decomposition is able to provide accurate modal data. Further, we need to investigate how the modal data behavior is related to the operation of the array, and whether it is a tool well suited for the study of electrically large antenna arrays.

We approach this work by reviewing the topic of CMA and applying it to two classes of antenna arrays. In Chapter 2 we provide an overview of CMA and note a number of concerns and open problems in its application. In Chapter 3 we apply CMA to linear arrays of resonant length rings in free-space. These arrays are very electrically large, with up to 40 elements, and are subject to grating-lobes. Chapter 4 address smaller half-wavelength dipole arrays, with some in the presence of finite rectangular ground-planes. Chapter 5 provides our conclusions from the accuracy analysis and suggestions for future work.

CHAPTER 2

METHOD OF MOMENTS AND CHARACTERISTIC MODE ANALYSIS

Central to this project's work is the use of characteristic mode analysis and the insight it offers the study of electromagnetic phenomena. In order to understand how the method can be utilized to optimize the design procedure of finite arrays we must first have a strong understanding of what the methodology is comprised of and the information it provides. In this section we provide an overview of characteristic mode analysis and define the values of interest that we will examine further and use to quantify our results in later sections. Additionally, we address the need for modal tracking algorithms and provide an overview of the ones we utilize.

2.1   CMA overview

Originally explored by Garbacz and Turpin [10], CMA was used to provide a general means of expanding radiated and scattered fields in electromagnetics problems featuring perfect electric conductors. The CMA method was deemed particularly useful because the basis over which the fields were expanded was entirely determined by the conductor's shape, and not by the method of excitation. Soon after its introduction the method was reformulated by Harrington and Mautz [11, 12] into a more general form, enabling the analysis of more geometrically complicated structures. To introduce the method we will summarize the formulation provided in [11], which considers a problem of conducting bodies with surface S and an impressed electric field $\mathbf{E}^i$. We define a current operator in the equation

$$\left[L(\mathbf{J}) - \mathbf{E}^i\right]_{\tan} = 0 \tag{2.1}$$

where $\mathbf{J}$ is the electric current on surface S and tan denotes the tangential components on S. In this form the generic L operator produces a field

intensity quantity from a provided current $\mathbf{J}$. Using this as an impedance operator we introduce the notation

$$Z(\mathbf{J}) = [L(\mathbf{J})]_{\text{tan}} \tag{2.2}$$

where Z is a symmetric operator which can be separated in the form $Z = R + jX$, resulting in R and X being both real and symmetric operators, respectively. Additionally, R is positive semidefinite as the power radiated by some current $\mathbf{J}$ on surface S is $\langle \mathbf{J}^*, R\mathbf{J} \rangle \geq 0$. In this work we have limited our scope to purely PEC problems in free space, which allows us to refer to Poynting's theorem

$$P_{\text{src}} = P_{\text{rad}} + j2\omega(\overline{W}_m - \overline{W}_e) \tag{2.3}$$

where

$$P_{\text{src}} = - \iiint\limits_{V} \vec{E} \cdot \vec{J}_i^* dV \tag{2.4}$$

$$P_{\text{rad}} = \oiint\limits_{S'} \left(\vec{E} \times \vec{H}^* \right) \cdot d\vec{s'} \tag{2.5}$$

and assert that the real part of the radiated power must be equal to the real part of the source power:

$$\text{Re}[P_{\text{rad}}] = Re \left[\oiint\limits_{S'} \vec{E}_m \times \vec{H}_n^* ds' \right] = \text{Re}[P_{\text{src}}]. \tag{2.6}$$

In order to solve our electromagnetic systems computationally we must adapt these formulas so that they can be applied to a discretized system. Using linear algebra notation we can represent the real radiated power as

$$\text{Re}[P_{\text{rad}}] = \text{Re}[P_{\text{src}}] = \text{Re}[(\vec{J}^*)^T \mathbf{Z} \vec{J}] = \vec{J}^T \mathbf{R} \vec{J} = \left\langle \vec{J}, \mathbf{R} \vec{J} \right\rangle. \tag{2.7}$$

Adapting some of the formulation from [10] a generalized eigenvalue problem is stated:

$$\mathbf{Z}(\vec{J}) = \nu \mathbf{R}(\vec{J}) \tag{2.8}$$

where $\nu = 1 + j\lambda$, formalizing that P_{src} is a complex multiple of $\text{Re}[P_{rad}]$.

Simplifying the problem:

$$(\mathbf{R} + j\mathbf{X})\vec{J} = (1 + j\lambda)\mathbf{R}\vec{J} \tag{2.9}$$

we arrive at the standard form of the characteristic mode eigenvalue problem

$$X(\mathbf{J}_n) = \lambda_n R(\mathbf{J}_n) \tag{2.10}$$

where, due to the properties of X and R, the eigenvalues λ_n and eigen-functions $\mathbf{J}_n$ must be real for any given mode number n. Additionally, the eigenfunctions $\mathbf{J}_n$, also referred to as eigencurrents, satisfy the orthogonality requirements

$$\begin{aligned} \langle J_m, RJ_n \rangle &= 0 \\ \langle J_m, XJ_n \rangle &= 0 \\ \langle J_m, ZJ_n \rangle &= 0 \end{aligned} \tag{2.11}$$

where $m \neq n$.

2.2   Modal solutions of excited structures

Once solved, we can use the eigenresults from Eq. (2.10) to derive a number of related values that can help describe the modal operation of a practical antenna design. Harrington shows that we can produce a modal analysis for a total current $\mathbf{J}$ on a structure by using the eigencurrents as both the expansion and testing functions in a MoM solution [13]. We do so by assuming that the $\mathbf{J}$, produced by some feed or incident wave, is a linear combination of weighted modal currents

$$\mathbf{J} = \sum_n \alpha_n \mathbf{J}_n \tag{2.12}$$

where α_n are the unknown weighting coefficients. After some manipulation and use of the orthogonal properties of the modal currents under the impedance operations we arrive at the relationship

$$\alpha_n(1 + j\alpha_n) = \langle J_n, E^i \rangle \tag{2.13}$$

where E^i is the incident excitation vector. The right side of Eq. (2.13) is referred to as the modal excitation coefficient and can be denoted as:

$$V_n^i = \langle J_n, E^i \rangle = \oiint_S \mathbf{J}_n \cdot \mathbf{E}^i ds.$$ (2.14)

The modal excitation coefficient represents how well an impressed field excites a given modal current $\mathbf{J}_n$. With the eigencurrents normalized to radiate unit power as

$$\langle J_m^*, RJ_n \rangle = \delta_{mn}$$ (2.15)

the total modal solution can be expressed as

$$\mathbf{J} = \sum_n \frac{V_n^i \mathbf{J}_n}{1 + j\lambda_n}.$$ (2.16)

Additionally we can utilize the complex Poynting theorem to show how the characteristic modes radiate power independently of one another:

$$
\begin{aligned}
P(J_m, J_n) = \langle J_m^*, ZJ_n \rangle &= \langle J_m^*, RJ_n \rangle + j \langle J_m^*, XJ_n \rangle \\
&= \oiint_{S'} \vec{E}_m \times \vec{H}_n^* ds + j\omega \iiint_{\tau'} \left(\mu \vec{H}_m \cdot \vec{H}_n^* - \epsilon \vec{E}_m \cdot \vec{E}_n^* \right) d\tau \\
&= (1 + j\lambda_n)\delta_{mn}
\end{aligned}
$$

(2.17)

where S' is any surface enclosing S and τ' is the space enclosed by S'. From Eq. (2.17) we see that positive and negative eigenvalues result in modes storing net magnetic of electric energies, respectively. Further we see that modes with eigenvalues of zero have an entirely real radiated power quantity, with these modes being called resonant.

Another commonly used metric is modal significance

$$\text{MS} = \left| \frac{1}{1 + j\lambda_n} \right|$$ (2.18)

which is a measure of the normalized amplitude of the modal currents [14]. Frequently used in the analysis of electrically small devices, the modal significance is used to determine which one or two modes are "dominant" on small structure. Additionally, the term is not dependent on the excitation vector.

Alternatively, we will focus on the modal current weight term, denoted as α_n in Eq. (2.12), and defined via Eq. (2.16) as

$$\alpha_n = \frac{V_n^i}{1 + j\lambda_n}. \tag{2.19}$$

This complex value helps provide a better look at the relative impact and properties of a given modal current, and how the modal eigencurrents are scaled due to a specified excitation.

2.3 Numerical accuracy concerns

As noted, modern applications of characteristic mode analysis are based on the solution of the characteristic mode generalized eigenvalue problem

$$\mathbf{XJ} = \lambda \mathbf{RJ} \tag{2.20}$$

where $\mathbf{X}$ and $\mathbf{R}$ are the imaginary and real parts, respectively, of the method of moments impedance matrix $\mathbf{Z}$. For lossless conductive structures, $\mathbf{Z}$ would ideally be symmetric. As such, $\mathbf{X}$ and $\mathbf{R}$ should be Hermitian-symmetric. However, we note that these ideal cases do not often hold in practice. In our work, we make use of the commercial solver FEKO, which we use to build our models and calculate our impedance matrices. Despite our structures being made entirely of perfect electric conductors, the calculated $\mathbf{Z}$ is often asymmetric. This may facilitate some of FEKO's more advanced MoM solver techniques, but it is non-ideal for CM applications. Additionally, as noted in one of the seminal works on characteristic mode analysis by Harrington and Mautz [11], any system is prone to numerical inaccuracy, which can degrade the measure of symmetry attainable for our MoM based approach. However, these problems can be partially mitigated by reconditioning methods which can force symmetry and positive semi-definiteness. We address these steps in further detail in Section 3.1.1.

2.4 Mode tracking over frequency

When studying characteristic modes over a range of frequencies, the Method of Moments impedance matrix Z must be calculated at each frequency point of interest. From the real and imaginary parts of Z we solve the characteristic mode eigenvalue problem. However, since there is no inherent correlation between multiple solutions over frequency, we must use a mode tracking algorithm in order to determine consistent modal designations across the frequency range. The process depends upon the idea that the modal decomposition changes slowly with frequency. As long as the frequency increment is small one should be able to classify like modes, even as they change slightly between independent solutions. While commercial solvers attempt to address the problem, there is no one best methodology for modal tracking. To address this issue we utilize an adapted form of the algorithm presented in [15]. Some direct methods attempt to track modes by following the eigenvalues of modes over frequency. Unfortunately, many antenna models support degenerate modes, which result in more than one mode having the same eigenvalue at a particular frequency, often causing direct tracking algorithms to lose track of modes. The modified method we apply relies on the eigenvectors of the CM problem. This method takes advantage of the fact that individual characteristic modes are orthogonal to one another through the impedance operators, R and X, as shown by

$$\left\langle \mathbf{J^i}, \mathbf{R}\mathbf{J^j} \right\rangle = \delta_{ij}, \tag{2.21}$$

where i and j are the indices of two characteristic modes. Using this property we correlate the modes by their eigencurrent distributions. To do so, we initially solve the problem at our first frequency point, freq_a, and then take the inner product of our eigencurrent with the set of eigencurrents calculated at the following frequency point, freq_b:

$$\left\langle \mathbf{J^i_{freq_a}}, \mathbf{R}\mathbf{J^j_{freq_b}} \right\rangle. \tag{2.22}$$

When a mode's inner product with a mode at the following frequency is high, we label it with the same modal index. Utilizing the inner product of eigencurrents produces significantly better tracking results than those found in our commercial solver; however, as demonstrated in Chapter 4 this method can

9

still struggle with larger problems. We note that while convention typically starts tracking modes from the low end of the frequency band of interest, our modified method can start tracking from any frequency point.

CHAPTER 3

LINEAR RING ARRAYS

Modal decomposition methods are useful tools in analyzing antenna structures and other radiation-based problems. One of the most thorough studies of finite antenna arrays is Bekers' "Finite Antenna Arrays: An Eigencurrent Approach"[16]. In this work Bekers analyzed finite linear antenna arrays of simple strip dipoles and thin wire rings. The methodology was based around constructing a representation of the total array's behavior by way of an iterative "cycling" process where single-element modes with perturbations were used as the bases for the total array currents. The author acknowledged the utility of characteristic mode analysis but opted to use an alternative decomposition that would allow a unit-cell type approach. As we have noted, a benefit of characteristic mode analysis is that it explicitly characterizes the entire conducting body as a whole, including the coupling behavior between elements. Consequently it incurs computational and storage costs when applied to an electrically large problem.

In this chapter we examine linear arrays of thin rings, similar to those studied in Bekers' past works [16, 17, 18]. The purpose of this section is to determine the achievable accuracy of a CM decomposition, and to see if the properties discerned in these past works are comparable to the results produced by CM analysis. Being able to draw correlations between the two analyses allows us to make use of this past research within the context of the resurgent field of CM analysis. We first examine how well the CM eigenvalue problem—often used in the study of electrically small antennas—is conditioned for our electrically large radiating structures.

3.1   Modal problem conditioning

The seminal works of Harrington and Mautz [12] noted the effects of non-ideal impedance matrix formulations on the CM eigenvalue problem. Recent work has explored these potential numerical problems at length [19] and has compared the discretized results of a moment-method solution to the modal results of a sphere, one of the few canonical structures one can study. As we are concerned with the interactions of multiple elements in a finite array, we perform similar tests on a set of linear arrays. Reproducing a model studied in [16] we simulate variations of a 40-ring linear array. We simulate the structure in the commercial solver FEKO and using in-house GPU accelerated MoM code [20] written in Python. The in-house solver uses Galerkin testing and RWG basis functions [21, 22]. The interactions between most basis function elements are processed using a 12-point quadrature rule. Green's function singularities, which arise in the case of a basis function overlap, are handled using Duffy integration in conjunction with an adaptive Gauss-Kronrod rule [22]. With both simulation tools we define the rings as infinitely thin PEC strips, discretized using the RWG basis functions [23]. Additionally in FEKO we construct a model in which the rings are defined as thin wires and simulated using a thin-wire kernel. The structural and meshing dimensions are specified per each simulation, where all electrical dimensions are with respect to $f_0 = 300$ MHz, at which a single ring is approximately 1λ long.

3.1.1   Single-ring antenna element

We begin by solving the CM problem for a single-ring element, with geometric variables as depicted in Figure 3.1. We model the ring as an infinitely thin PEC strip in the FEKO modeling tool, with an impressed voltage source implemented on an edge port. We then use FEKO to generate an impedance matrix of the structure. Additionally, we use the exported geometry data from FEKO and reproduce the structure in our in-house MoM solver. Last, we use FEKO to produce an impedance matrix for a similarly sized ring, using a thin-wire kernel implementation. With these three different impedance matrix calculations, we solve the CM eigenvalue problem of Eq. (2.10) and then compare the accuracy of our modal sum currents to the currents from
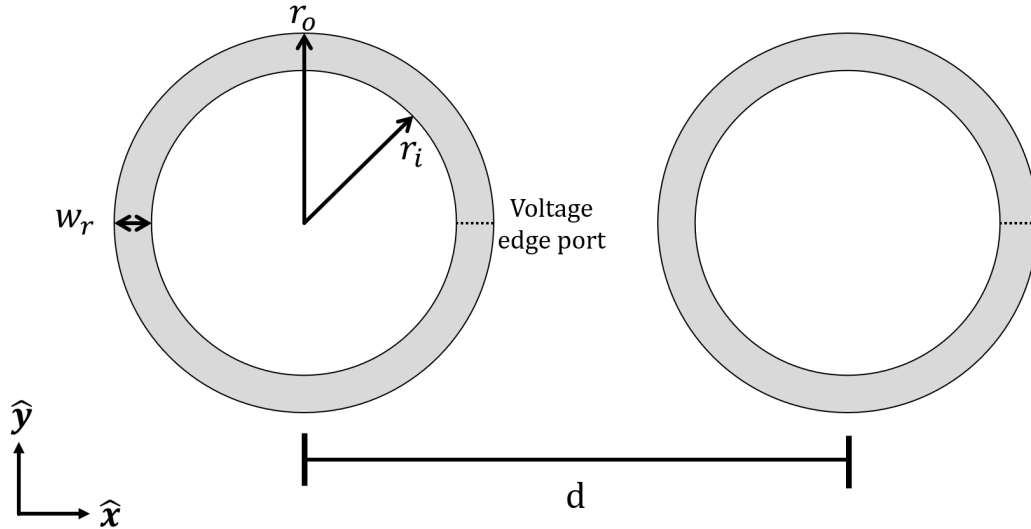
Figure 3.1: A single thin-strip ring with relevant dimensions (ring width w_r, outer radius r_o, inner radius r_i, inter-element spacing d). The dotted segment represents the location of the voltage edge port.

a direct MoM solution.

Concurrent work by Guan et al. [24] defines an ℓ^2 norm percent error for a total modal current distribution compared to a standard MoM solution. Modified to fit with our established notation, this total current percent error quantity is defined for the real and imaginary current components as

$$\text{Real error}(m) = 100 \cdot \frac{\left|\Re(\mathbf{J}_{\text{modal}(m)}) - \Re(\mathbf{J}_{\text{driven}})\right|_2}{\left|\mathbf{J}_{\text{driven}}\right|_2} \tag{3.1}$$

and

$$\text{Imaginary error}(m) = 100 \cdot \frac{\left|\Im(\mathbf{J}_{\text{modal}(m)}) - \Im(\mathbf{J}_{\text{driven}})\right|_2}{\left|\mathbf{J}_{\text{driven}}\right|_2} \tag{3.2}$$

where $\mathbf{J}_{\text{modal}(m)}$ is the complex current vector of the modal summation Eq. (2.16) of m-many modes, and $\mathbf{J}_{\text{driven}}$ represents the complex current vector resulting from a standard MoM driven solution, with the ℓ^2 norm defined for some vector $\mathbf{x}$ as

$$|\mathbf{x}|_2 = \sqrt{\sum_{k=1}^{n} |x_k|^2}. \tag{3.3}$$

13

Additionally we present a total error quantity defined as

$$\text{Total error}(m) = 100 \cdot \frac{\left|\mathbf{J}_{\text{modal}(m)} - \mathbf{J}_{\text{driven}}\right|_2}{\left|\mathbf{J}_{\text{driven}}\right|_2} \tag{3.4}$$

We wish to see how many modes must be included in Eq. (2.16) in order to achieve a suitably accurate modal sum. Additionally, we compare the accuracy of our modal sums using impedance matrices (1) as they are originally produced, (2) that are symmetrized after being produced, and (3) that are symmetrized and recomposed to be positive definite. As noted in Section 2.3, our impedance matrices would ideally be symmetric and positive definite, and certain modal properties are dependent upon these conditions. Addressing this *ex post* in cases 2 and 3, the impedance matrix can be symmetrized as

$$\mathbf{Z}_{\text{sym}} = \frac{1}{2}\left(\mathbf{Z} + \mathbf{Z}^T\right). \tag{3.5}$$

Indefiniteness of the real part of the impedance matrix is addressed by decomposing the $\mathbf{R}$ matrix as

$$\mathbf{R}\hat{\mathbf{I}}_n = \xi_n\hat{\mathbf{I}}_n \tag{3.6}$$

and replacing negative eigenvalues in ξ with the value zero. The resistance matrix is then recomposed as

$$\mathbf{R}_{\text{pos}} = \hat{\mathbf{I}}\xi\hat{\mathbf{I}}^T \tag{3.7}$$

where ξ is a diagonal matrix of the modified eigenvalues, with negative values set to zero. Unless stated otherwise, any use of the resistance matrix in this work is referring to the post-processed $\mathbf{R}_{\text{pos}}$ positive-definite version of Eq. (3.7).

Figure 3.2 shows the total current percent errors calculated for four similar thin-strip ring models, as simulated by FEKO, with separate error values calculated for the real and imaginary components of our currents. "Orig" indicates a solution using the original impedance matrix. "Sym" indicates that the matrix was made symmetric via Eq. (3.5). "SPD" indicates that the matrix was made symmetric and positive-definite via Eq. (3.7).

Most interestingly we see that composing a modal sum using the original direct solution to the CM eigenvalue problem produces dramatically inaccurate currents. This behavior is unexpected and indicates a fundamental issue

14

with directly performing a CM decomposition on the raw impedance matrix from FEKO. This particular behavior is due to the the physical degrees of symmetry in the single element. Comparison cases and comments can be found in Appendix A. Symmetrizing the impedance matrix improves the accuracy in all cases. If we further condition our impedance matrix and re-compose it such that it is positive definite, we observe varying results across our four model variations. In variations 1 and 4 we observe that forcing positive definiteness results in the most accurate modal sums, with regard to both the real and imaginary current components. Variations 1 and 4 of these ring models are made of thin strips with width $w_r = \lambda/100$. Variation 2 shows a significant reduction of accuracy from enforcing positive definiteness relative to the "only symmetrized" case. Variation 3 appears to encounter a minimum error floor, with enforcing positive definiteness only granting a minimal increase in accuracy. This overall comparison shows how sensitive a CM decomposition can be to the relationship between the problem geometry and mesh density. Furthermore it shows that care must be taken when using the output information from a commercial solver and how one must perform additional problem conditioning. The CM problem is often presented in a "plug-and-play" manner where the user only requires the impedance matrix of a structure, but even for a single ring with $ka \approx 1$ we witness inaccuracy that must be reduced with proper care. From these results we will choose to work with the dimensions used in variation 4 and enforce symmetry and positive definiteness on our impedance matrices. For a single array element this results in the best modal sum accuracy where only the first two modes are needed for $\mathrm{Re}(\mathbf{J})$ error minimization. Additionally, the $\mathrm{Im}(\mathbf{J})$ component is slower to converge in most CM decompositions, with this being more apparent in larger examples presented later. This behavior is consistent with past analyses of strip dipoles [25]. The total current percent errors for the complete modal sums of the thin-strip ring are shown in Table 3.1.

Using the same thin-strip ring geometry we calculate our impedance matrices using our in-house MoM code. Again we calculate the total current percent error for the original matrix, symmetrized matrix, and symmetric positive definite matrix, with the results shown in Figure 3.3. In contrast to the FEKO matrix related results in Figure 3.2, here we note that the original matrices do produce reasonable results, and in two geometry variations they produce the most accurate modal current summations. Similar to
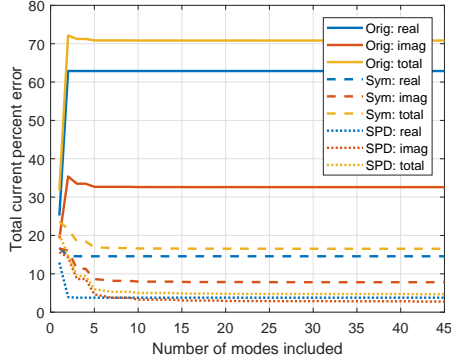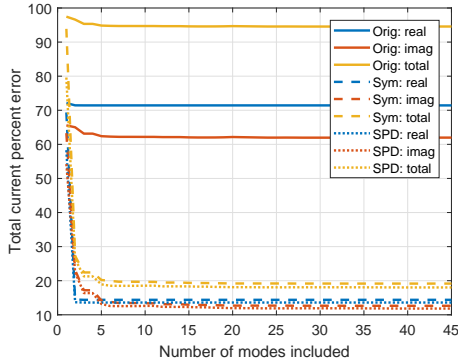
15
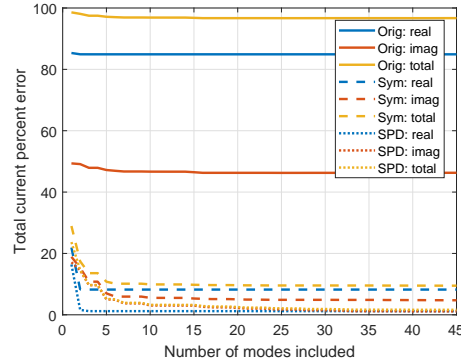
(a) Variation 1:
$w_r = \lambda/100; \; m_l = \lambda/60$
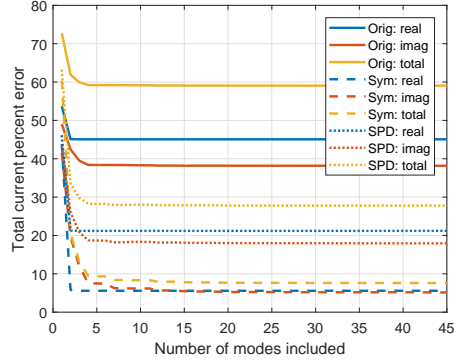
(b) Variation 2:
$w_r = \lambda/50; \; m_l = \lambda/60$

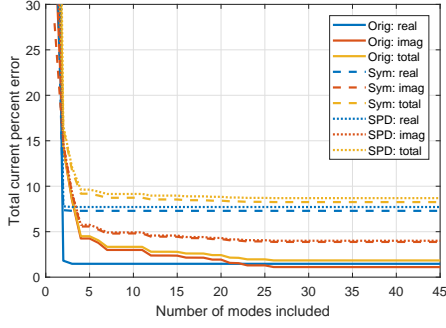(c) Variation 3:
$w_r = \lambda/50; \; m_l = \lambda/30$

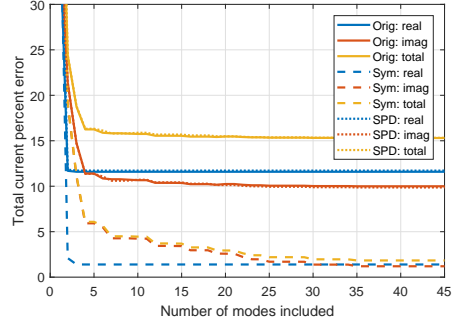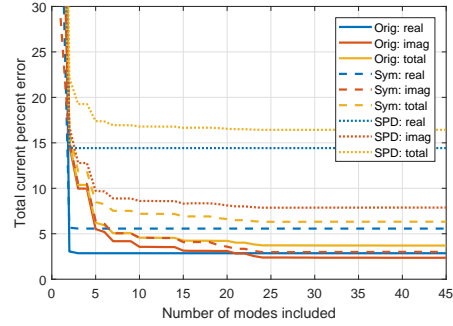(d) Variation 4:
$w_r = \lambda/100; \; m_l = \lambda/30$

Figure 3.2: Total current percent error values calculated according to Eqs. (3.1) and (3.2) for a single thin-strip ring simulated in FEKO. Four ring variations were tested, with differing ring widths (w_r) and maximum mesh edge lengths (m_l), using the original impedance matrix, and two *ex post* conditioned matrices.

Table 3.1: Total current percent error values calculated according to Eqs. (3.1) and (3.2) for the thin-strip rings of Figure 3.2 with all modes included. The values represent the real/imaginary errors, respectively.

Ring Model	Original Error	Sym Error	Sym and Pos Def Error
FEKO Var 1	62.87 / 32.60	14.57 / 7.80	3.78 / 2.76
FEKO Var 2	45.08 / 38.17	5.58 / 5.14	21.20 / 17.95
FEKO Var 3	71.43 / 61.98	14.39 / 12.65	13.59 / 11.83
FEKO Var 4	84.90 / 46.29	8.22 / 4.74	1.19 / 1.12

16

(a) Variation 1:
$w_r = \lambda/100; m_l = \lambda/60$

(b) Variation 2:
$w_r = \lambda/50; m_l = \lambda/60$
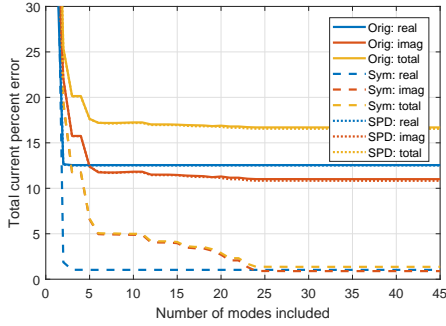
(c) Variation 3:
$w_r = \lambda/50; m_l = \lambda/30$

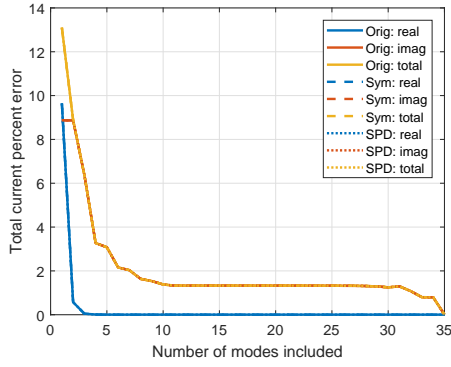(d) Variation 4:
$w_r = \lambda/100; m_l = \lambda/30$

Figure 3.3: Total current percent error values calculated according to Eqs. (3.1) and (3.2) for a single thin-strip ring simulated using in-house MoM code. The y-axis values are truncated to better demonstrate the differences between the results. Single mode error in all cases is 100%.

the FEKO case, the modal currents of the thinner strip rings (variations 1 and 4) achieve the most accurate modal representations; however, with the in-house formulation the original matrices provide the most accurate results. In variations 2 and 3 we observe the symmetrized case resulting in the least error, and original and positive definite matrices resulting in almost identical modal accuracies. Finally, in none of the geometry and mesh variations does the positive definite impedance matrix produce the best results, running contrary to the results of the previous simulations and intuition. The accuracy values of the complete modal sum are presented in Table 3.2.

When simulating wire antennas it is often acceptable to use a thin-wire kernel where we assume only current tangential to the wire exists. A wire "thickness" value can be included to increase the accuracy of the simulation and to help avoid singularities when evaluating overlapping wire segments.

Table 3.2: Total current percent error values calculated according to Eqs. (3.1) and (3.2) for the thin-strip rings of Figure 3.3 with all modes included. The values represent the real/imaginary errors, respectively.

Ring Model	Original Error	Sym Error	Sym and Pos Def Error
In-house Var 1	1.47 / 1.11	7.29 / 3.87	7.71 / 4.00
In-house Var 2	11.59 / 9.99	1.39 / 1.20	11.72 / 9.87
In-house Var 3	12.55 / 11.01	1.03 / 0.89	12.51 / 10.83
In-house Var 4	2.86 / 2.36	5.57 / 3.01	14.42 / 7.88

(a) $s_l = \lambda/30$; $r_w = \lambda/2000$
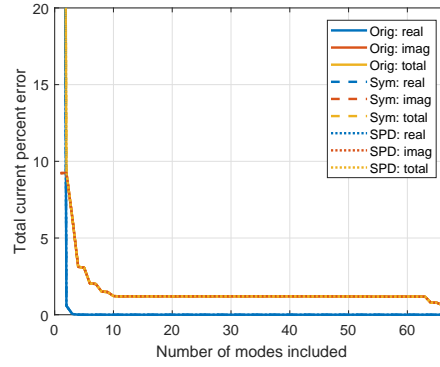
(b) $s_l = \lambda/60$; $r_w = \lambda/2000$

Figure 3.4: Total current percent error values calculated according to (3.1) and (3.2) for a single thin-wire ring simulated in FEKO. Two ring variations were tested, with differing wire segment lengths (s_l), both with constant wire radii (r_w).

Using FEKO we produce impedance matrices for two variations of a thin-wire ring comparable to the thin-strip models analyzed previously. Figure 3.4 depicts the current error for the two models with varying segment lengths. One key distinction in the wire case can accurately represent both the real and imaginary components of the current distribution, with both summations achieving zero error. However, while the real component only requires the sum of two modes, the imaginary error drops quickly and then stays constant until we include the higher order currents contributed by the very last few modes of the summation. This behavior is distinct from both RWG-based models, where the imaginary part of the error decreases over the entire range of included modes, albeit slowly.

Having simulated our single ring element using three different methods and four different discretized geometries, we make the following conclusive observations.

1. The FEKO RWG formulation of a thin-strip ring requires reconditioning in order to make the results usable. Further, additional conditioning does not guarantee suitable accuracy of the modal sum for all applications and comparisons. This is best seen in the decompositions of variations 2 and 3 of the FEKO formulation, as shown in Figures 3.2b and 3.2c. We note that the thinner models attain a higher accuracy in general.

2. The in-house formulation can be degraded by forcing additional constraints such as symmetry and positive definiteness. As shown in Figures 3.3a and 3.3d, the original impedance matrix produces the most accurate modal decomposition. Figures 3.3b and 3.3c show the symmetrizing the impedance matrix results in increased accuracy, but forcing positive definiteness severely degrades it.

3. The thin-wire kernel can provide a perfect match to the equivalent driven current solution, both in terms of real and imaginary error components. However, to achieve an accurate imaginary current component the highest order modes must be included.

Expanding on these points we note that one general trend observed for the RWG models is that the percent error is minimized rapidly by the inclusion of the first few modes. The total current error then typically reaches its absolute

minimum once approximately 25 modes are included. One significant outlier is the imaginary component of the thin-wire kernel error, where the error appears to reach a consistent value once 11 modes are included. However, it is only once the last four modes are added that we see an additional drop in the model's error. This unusual behavior demonstrates the influence of characteristic mode ordering and potential oversights related to reduced order modeling. Our modal indices are determined by the magnitude of the corresponding modal eigenvalue, as is typically the convention in CM. Lower-order modes are designated as more modally significant by definition, as shown in Eq. (2.18). Convention leads us to believe that lower-order modes therefore contribute most strongly to a modal sum's accuracy, with higher-order modes providing small adjustments. As we see in the thin-wire case however, the higher-order modes of even this simple ring element are essential to the modal sum accuracy. Were we to only solve for a reduced set of modes, we could potentially omit these final modes and assume that the missing currents were simply outside the range of the characteristic mode basis.

As noted, for all cases of the in-house solver, and in variation 2 of the FEKO model, enforcing positive-definiteness reduces the maximum attainable accuracy of the model, relative to one that is simply symmetrized. This can be due to the fact that forcing positive-definiteness essentially "zeros" out the offending components of the impedance matrix. If one were to relax the constraint and keep modes associated with negative but very low magnitude $\mathbf{R}$ eigenvalues, those modes may be able to contribute to the accuracy of the greater modal sum. However, as a matter of definition the mode would no longer be a true characteristic mode. Modified formulations of characteristic modes often have to relax these constraints, especially when attempting to include dielectrics [26].

Additionally, we note a special consideration that may arise when computing these results using standard eigenvalue solvers. In this work we use the MATLAB function `eig()` to solve one-sided and generalized eigenvalue problems. By default the function will perform checks on the condition of the problem and use different eigenvalue problem solution algorithms depending on the result. For our set of problems we note that the matrix $\mathbf{R}$ is poorly conditioned. In this case `eig()` would use the QZ algorithm to perform the decomposition. However, when we recompose our matrix and force it to be

symmetric, the solver will use the Cholesky decomposition which will produce inaccurate results. In this case it is important to force the use of the QZ algorithm. Further, we note that even reconditioned impedance matrices and QZ decomposition can lead to numerically complex eigenvalues and eigenvectors in some cases. In all of our simulations we discard the imaginary component of the eigendata, and discard the mode entirely if the returned eigenvalue is infinite.

3.1.2 Variable length linear arrays

Having examined the single-ring element, we proceed to study linear arrays of 5, 10, 20, 30, and 40 ring elements. The total current error metrics of a single ring indicated that the conditioning of the resistance matrix $\mathbf{R}$ had a dramatic effect on the accuracy of a modal sum. Past work [19] has shown that the indefinite nature of calculated $\mathbf{R}$ matrices is largely due to finite precision limitations. Alternative formulations making use of spherical wave expansions of the dyadic Green function have shown promise in reducing numerical difficulties in the decomposition [27]. However as most CM implementations, both commercial and research oriented, make use of the EFIE method and the free-space electric field Green function, we restrict our focus to these methods and how they perform when applied to electrically large array problems.

Revisiting the $\mathbf{R}$-matrix eigenvalue problem, $\mathbf{R}\hat{\mathbf{I}}_n = \xi_n\hat{\mathbf{I}}_n$, for a range of different array sizes we determine how many of the eigenmodes are associated with either negative or complex eigenvalues. Negative eigenvalues indicate negative radiated power, with the associated eigencurrents $\mathbf{I}_n$ causing $\mathbf{I}_n^H\mathbf{R}\mathbf{I}_n \leq 0$. These modes arise from numerical noise. Asymmetry in $\mathbf{R}$ results in undesirable complex eigenvalues. With these undesired cases specified, we regard modes that produce positive and real eigenvalue as "valid." We present the number of eigenvalues with these properties in Table 3.3, for non-symmetrized matrices directly produced by FEKO. In tabulating the results we noted that the undesired properties are not exclusive of each other. In this table we present results for two frequencies, comparing when a single ring has $ka \approx 0.5$ and $ka \approx 1$. This is to provide additional context, considering most CM simulations are done on electrically small elements. Besides

Table 3.3: Properties of eigenvalue solutions from Eq. (3.6) for non-symmetrized matrices produced by FEKO.

N_{array}	N_{edges}	ka	Negative Re(ξ)	Complex ξ	Valid ξ
1	60	.52/1.04	17/15	30/38	21/15
5	300	4.29/8.58	251/224	222/282	98/91
10	600	9/18.00	247/220	388/412	135/146
20	1200	18.42/36.84	525/457	868/846	199/277
30	1800	27.84/55.67	800/691	1364/1284	260/399
40	2400	37.26/74.51	1071/935	1808/1710	379/531

the initial case of a single ring we note that all of the results are for very electrically large structures, where ka is designated by the total array's largest dimension. This is an important point as the MoM impedance matrix is calculated on the entire structure, and not built using an element cell method. While expensive computationally, this approach is most likely to capture the inter-element coupling behavior of the array.

Symmetrizing the FEKO matrices by (3.5) we evaluate the **R** matrix eigenvalue problem and gather the results shown in Table 3.4. We see that symmetrizing the impedance matrix completely removes the complex eigenvalues, and while there is a slight increase in negative real eigenvalues, overall there is a net gain of valid values. This effect is most noticeable when comparing the valid eigenvalues of the 40 element array, showing the importance of reconditioning the impedance matrix of very electrically large problems. We note that symmetrizing the impedance matrices removes the complex eigenvalues but has the effect of adding to the number of eigenvalues with negative real parts. Despite this shift in undesirable properties, the net effect is a gain in the number of valid modes. As a comparison, we perform the same decompositions using our in-house MoM code, with the results cataloged in Tables 3.5 and 3.6. The results show how sensitive the **R** conditioning is to variations in its formulation. Entries marked with a "—" indicate that the solver failed to solve the eigenvalue problem, which is a shortcoming of the in-house code that is currently being worked on.

Table 3.4: Properties of eigenvalue solutions from Eq. (3.6) for *ex post* symmetrized matrices originally produced by FEKO.

N_{array}	N_{edges}	ka	Negative Re(ξ)	Complex ξ	Valid ξ
1	60	.52/1.04	22/18	0/0	38/42
5	300	4.29/8.58	126/110	0/0	174/190
10	600	9/18.00	260/233	0/0	340/367
20	1200	18.42/36.84	533/483	0/0	667/717
30	1800	27.84/55.67	809/736	0/0	991/1064
40	2400	37.26/74.51	1083/985	0/0	1317/1415

Table 3.5: Properties of eigenvalue solutions from Eq. (3.6) for non-symmetrized matrices produced by in-house MoM code.

N_{array}	N_{edges}	ka	Negative Re(ξ)	Complex ξ	Valid ξ
1	60	.52/1.04	3/0	20/24	39/36
5	300	4.29/8.58	27/3	194/144	101/155
10	600	9/18.00	73/13	446/348	147/249
20	1200	18.42/36.84	—/39	—/776	—/421
30	1800	27.84/55.67	—/57	—/1204	—/589
40	2400	37.26/74.51	—/88	—/1646	—/744

Table 3.6: Properties of eigenvalue solutions from Eq. (3.6) for *ex post* symmetrized matrices originally produced by in-house MoM code.

N_{array}	N_{edges}	ka	Negative Re(ξ)	Complex ξ	Valid ξ
1	60	.52/1.04	3/0	0/0	57/60
5	300	4.29/8.58	41/15	0/0	259/285
10	600	9/18.00	105/39	0/0	495/561
20	1200	18.42/36.84	—/94	—/0	—/1106
30	1800	27.84/55.67	—/145	—/12	—/1643
40	2400	37.26/74.51	—/203	—/22	—/2175

3.2 Array modal accuracy and beam steering

So far we have examined the accuracy of the modal current summation terms associated with individual antenna elements. Following [16] we now construct a large linear array of 40 rings, aligned along the element H-plane, as depicted in Figure 3.1. The inter-element spacing is $3\lambda/5$. With uniform amplitude and phase the array pattern is directed towards broadside. Examining our current error metric in Figure 3.5, we make note of some key properties.

1. For all three matrix conditions the real part of the error drops precipitously with the inclusion of mode 80.

2. The matrix conditioning has no strong effect on the real error component.

3. The matrix conditioning only affects the imaginary error component past the inclusion of 370 modes.

4. The addition of modes 91 through 129 results in an increase in the imaginary error component.

5. The symmetric and positive definite impedance matrix results in the most accurate decomposition. This is consistent with the results for a single element with the same geometry and meshing.

When studying a single antenna element such as a dipole or loop, the error in total structure current can be a useful metric. However as we move to multiple arrays an error metric that is based on port impedance values becomes more useful. We define total structure impedance (TSI) error as

$$\text{TSI error}(m) = 100 \cdot \frac{\left| \mathbf{Z}_{\text{modal}(m)} - \mathbf{Z}_{\text{driven}} \right|_2}{\left| \mathbf{Z}_{\text{driven}} \right|_2} \tag{3.8}$$

where $\mathbf{Z}$ is a vector of complex port impedances of length n, and $\mathbf{Z}_{\text{modal}(m)}$ is the impedance seen at port resulting from a modal sum of m-many modes. The metric is interpreted as the average percent error in port resistance or reactance one can expect from the modal-sum representation of the array's current distribution. This can serve as a direct means of determining if a modal-sum current is suitably accurate for an array developer, as performance specifications and array feed considerations may require improved
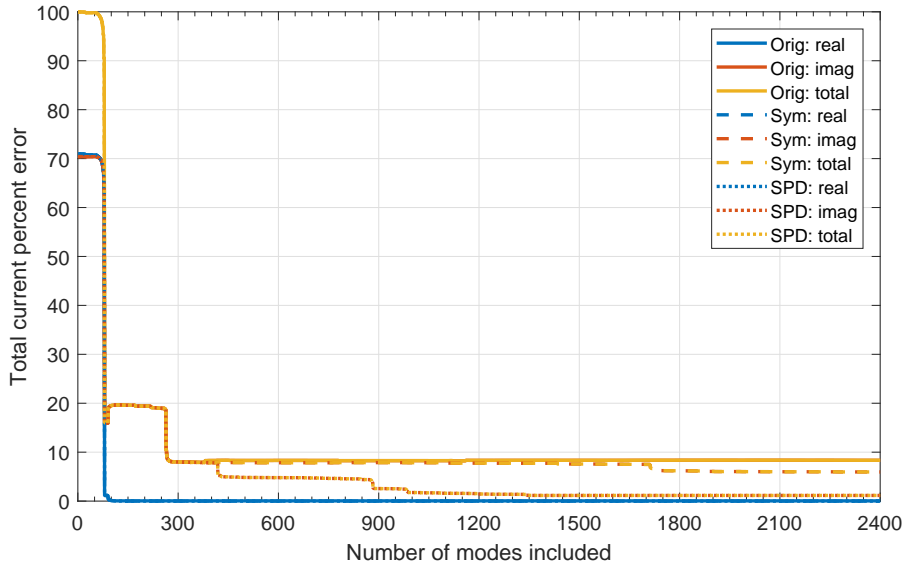
Figure 3.5: Total current percent error of a 40-element linear ring array $(d = 3\lambda/5)$ with different impedance matrix conditioning. The array elements are excited with uniform amplitude and phase.

accuracy. In Figure 3.6 we examine the real and imaginary TSI components for the symmetric and positive definite case of the array studied in Figure 3.5. The x-axis is limited since the addition of modes past 1500 does not result in a change in TSI. We observe that the inaccuracy of the imaginary current component translates to error in the real impedance component.

3.2.1 Beam steering effects

Up until this point we have only examined arrays that are uniformly excited for broadside radiation. Figure 3.7 depicts the total current percent error for the 40-element linear array as the main beam is steered in small increments from broadside. We note that no significant changes in error occur past the inclusion of 1500 modes. Two distinct effects are identified from the displayed results:

1. As shown in Figure 3.7a, the real component of the current error is incredibly sensitive to the scanned beam angle. A slight deviation from broadside excitation results in a "notch" effect, where the current error increases for a number of added modes.
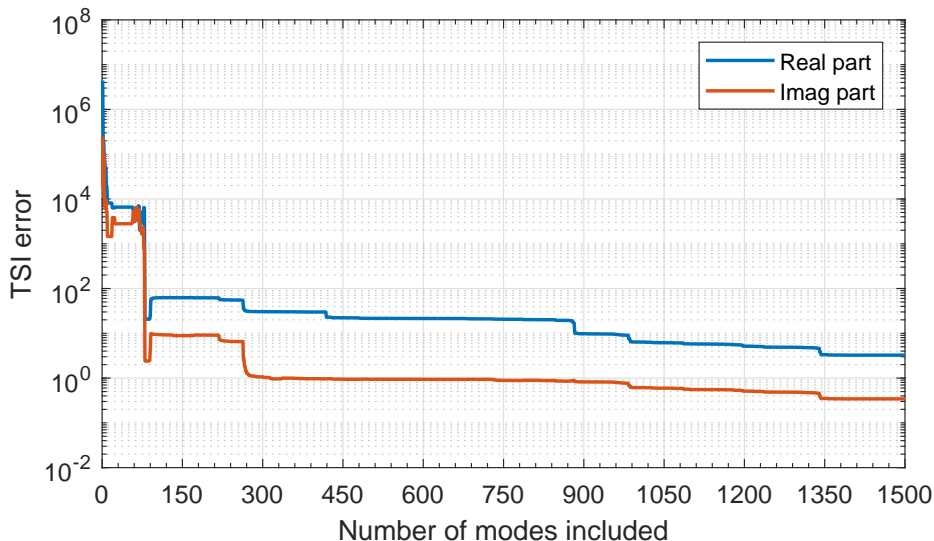
Figure 3.6: Real and imaginary parts of the TSI error (3.8) of a 40-element linear ring array ($d = 3\lambda/5$) with a symmetric and positive definite impedance matrix.

2. As shown in Figure 3.7b, steering 0.5° from broadside results in an increase in the imaginary current component. However, further slight increases, from 1° to 2°, reduce the imaginary current error.

In order to determine which modes contribute most to the modal sum quantity and how they may correlate with the current error values, we plot the magnitude of the complex modal weights [Eq. (2.19)] for the five scan angles, as shown in Figure 3.8. This plot is limited to the first 120 as all further values produce very low magnitude weights. From these results we can note that mode 80 is the major contributing current in a broadside excitation, an observation consistent with the current error metrics already shown.

3.2.2 Modal far-field accuracy

In addition to studying the weighted sums of eigencurrents, we can also examine the corresponding modal far-fields of the CM eigencurrent summations. For the linear array we are examining, we scan the beam along the array H-plane, which in this case is a cut-plane in xz. We then sample the far-field across $\theta = -90° : 90°$ in one-quarter degree increments. We define a modal
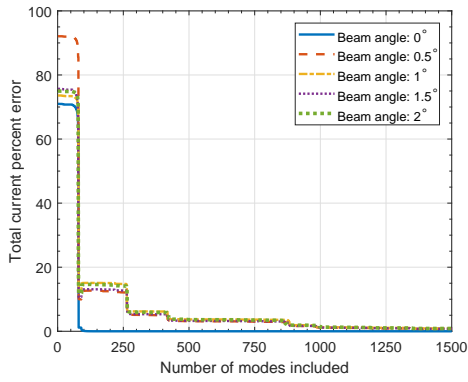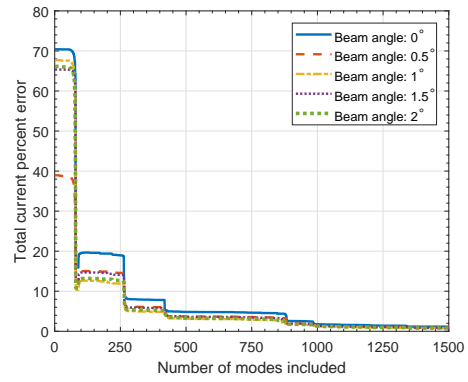
(a) Error in Re(**J**).   (b) Error in Im(**J**).

Figure 3.7: Current percent error of a 40-element linear ring array ($d = 3\lambda/5$) with excitations for five different beam angles relative to broadside.
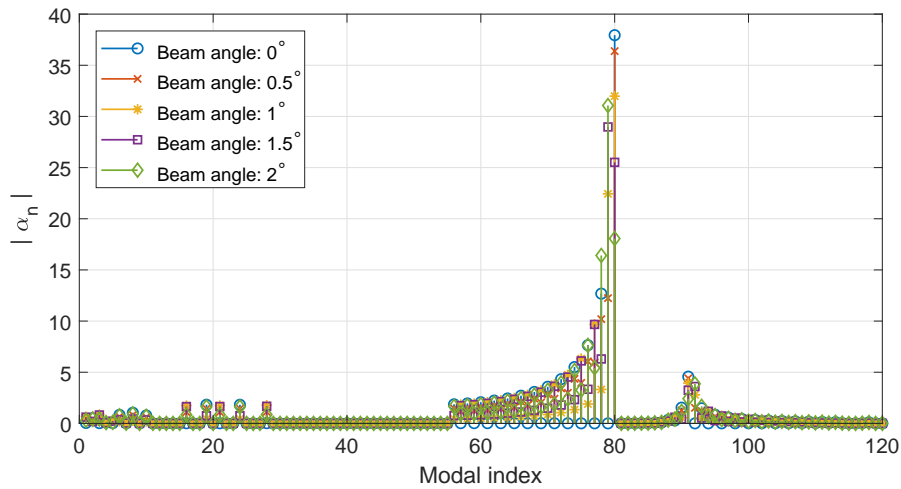
Figure 3.8: The magnitude of the modal weight coefficients of the 40-element linear ring array for five minor variations in beam angle.

far-field error metric as

$$\text{Far-field error}(m) = 100 \cdot \frac{\left|\mathbf{E}_\phi(\theta)^{\text{modal}(m)} - \mathbf{E}_\phi(\theta)^{\text{driven}}\right|_2}{\left|\mathbf{E}_\phi(\theta)^{\text{driven}}\right|_2} \qquad (3.9)$$

and note that the array radiation is almost entirely ϕ oriented, making it the E-field component of interest. Following from the fine scan angle adjustments shown in Figure 3.7, we proceed to examine the corresponding far-field error behavior, as depicted in Figure 3.9. Similarities and contrasts between the error metrics include:

1. The array current accuracy was very sensitive to scan angle; however, we see that the far-field accuracy is resilient.

2. The far-field percent error and the real current percent error decrease in a similar fashion. In both cases the inclusion of mode 80 drastically reduces the error, as the real current percent error drops from 89.90% to 1.63%, and the far-field percent error from 42.90% to 0.98%.

3. The addition of modes 82 through 90 results in an increase in far-field error for a broadside excitation. Similar behavior occurs for the other small beam scan angles. These trends are more easily seen in Figure 3.9b. This behavior mimics the increase seen in the imaginary current error.

The discrepancy between the error minimization rate of the modal eigencurrents and that of the modal far-fields is due to the orthogonality constraints established in the original CM problem formulation. Characteristic modes by definition are orthogonal through the $\mathbf{R}$ matrix, making their far-fields orthogonal to one another. Because orthogonality is ideally enforced on the far-field sphere, inaccuracy in the solution manifests in the near field and modal currents. It is possible to enforce orthogonality on the surface of the radiating structure, creating a set of orthogonal modal currents [28]. In such a case the currents would minimize in error more rapidly than the modal far-fields.

(a) Far-field error.　　　　(b) Zoomed in view of first 500 values.
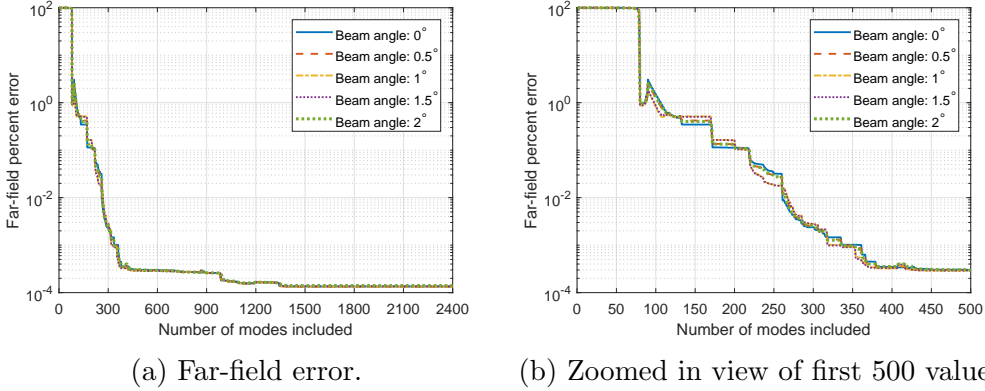
Figure 3.9: Far-field error [Eq. (3.9)] of the array and excitations examined in Figure 3.7

3.2.3　Modal attribution and scan behavior

Following Bekers' methodology [16] we select a set of scan angles that will result in grating lobes entering the visible region of the array. With his decomposition method one could specify modal far-fields that exhibited main lobes in the direction of a scan angle and in the direction of the emerging grating lobe. Using CM and a decomposition of the entire linear array as a single conducting body, we examine the scan behavior of the array and determine if similar behavior can be directly attributed to specific array eigencurrents. To determine our scan angles of interest we calculate and plot the array factor of our 40 ring array with $3\lambda/5$ spacing:

$$\text{AF} = \sum_{n=1}^{N_{\text{el}}} w_n e^{j2\pi(n-1)\frac{d_x}{\lambda}(u-u_s)} \tag{3.10}$$

where w_n is a unit value weight, and u and u_s are the simplified u-v projection values of our scan range where $u = \sin\theta$. Using a linear phase progression we scan the array from broadside at 0° to 90° and plot the magnitude of the array factor over the $\theta = -90° : 90°$ half-space, as shown in Figure 3.10. The linear pattern on the right side of the plot illustrates the main beam of the array being swept from broadside. The semi-circular segment on the left side of the figure shows an additional main beam entering the visible region of the array as an undesired grating lobe. Once we perform the CM decomposition

29

we can calculate the power radiated by our modal sum by computing

$$\left\langle \mathbf{J}^*_{\text{modal}(m)}, \mathbf{R}\mathbf{J}_{\text{modal}(m)} \right\rangle = P_{\text{rad}(m)} \tag{3.11}$$

where $\mathbf{J}_{\text{modal}(m)}$ is the current vector of the modal summation [Eq. (2.16)] of m-many modes. The resulting values are presented as a percentage of the power radiated by the standard driven solution and are displayed in Figure 3.11. Starting from broadside at $0°$ we see that very little power is radiated by the first approximately 80 modes. As we steer away from broadside we see power contributed by lower-order modes, with there being a near linear relationship until approximately $35°$ from broadside. At $30°$ the summation requires 58 modes in order to capture more than 95% of the radiated power. At $35°$ the power behavior changes dramatically, with only 24 modes being needed to capture 95% of the radiated power. This change coincides with the emergence of the secondary grating lobe, as indicated in Figure 3.10. This would indicate that as power is radiated in more simultaneous directions, power is better supported by lower order modes. We note that the order in which modes are included is solely determined by the magnitude of their corresponding eigenvalues. As such, we see that the broadside pattern of our array cannot "make use" of the lower order modes to radiate power. Furthermore, reiterating what was shown in Figure 3.5 we note that the lower order modes do not contribute to the current accuracy either at broadside.

Following [16] we proceed to examine four specific scan angles which result in grating lobes entering the visible region. We then identify which modal far-fields have main and secondary lobes that are best aligned with the desired scan angle and expected grating lobe angles. By inspection we note that the modes that best characterize the scan behavior are as follows:

1. Mode 3 produces a main lobe at $\pm 41.8°$ and secondary lobe at $\mp 90°$, corresponding the array's scan and resulting grating lobe angles.

2. Mode 5 produces a main lobe at $\pm 47.3°$ and secondary lobe at $\mp 68.9°$, corresponding the array's scan and resulting grating lobe angles.

3. Mode 10 produces a main lobe at $\pm 53.1°$ and secondary lobe at $\mp 60.1°$, corresponding the array's scan and resulting grating lobe angles.

4. Mode 11 produces a single main lobe at $\pm 56.2°$ corresponding to both
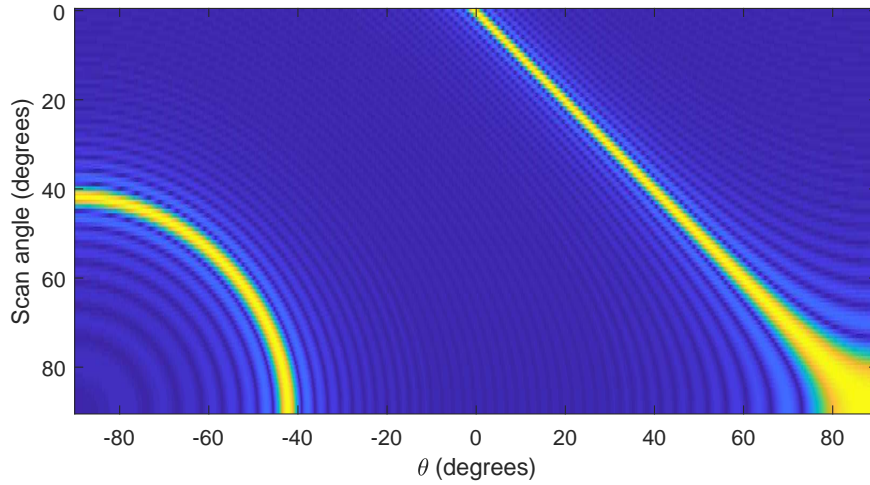
Figure 3.10: Array factor [Eq. (3.10)] magnitude of the 40-ring linear array with $3\lambda/5$ spacing. The array is phased with a linear phase progression from $0°$ to $90°$ from broadside, with the AF shown over the $\theta = -90° : 90°$ half-space.
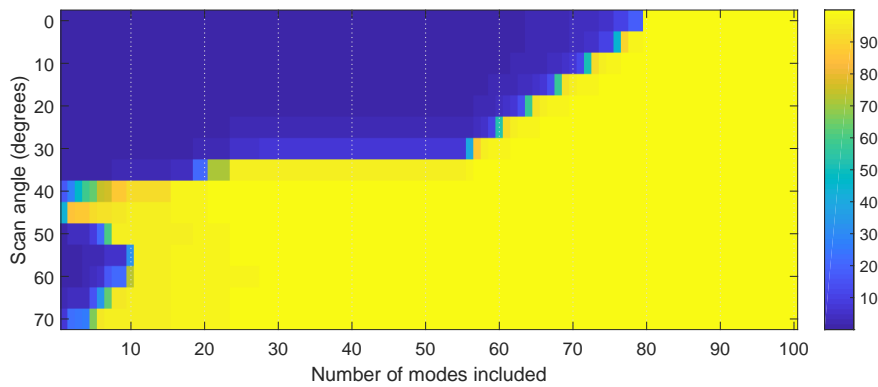

Figure 3.11: Power radiated by the modal sum current as a percentage of the power radiated by the port-driven solution.

Table 3.7: Total current percent error [Eqs. (3.1) and (3.1)] values for the linear ring array at broadside and scanned to 41.8° with all modes included. The values represent the real/imaginary errors, respectively.

Scan Angle	Original Error	Sym Error	Sym and Pos Def Error
0°	0.04412 / 8.34	1.029e-07 / 5.957	6.838e-08 / 1.156
41.8°	4.472 / 3.333	1.322 / 1.247	0.7105 / 0.6088

the array's scan angle and grating lobe angles at $\mp 56.2°$.

To ensure that the current accuracy behavior near broadside still applies once grating lobes enter the visible region, we scan our array to our first test point of 41.8° and compare the total current percent error for our array under different impedance matrix conditionings, as shown in Figure 3.12, with the minimum error values of a full solution shown in Table 3.7. We see a number of differences between these results and the broadside case in Figure 3.5.

1. The real current error is strongly affected by the matrix conditioning, with further treatment resulting in quicker error minimization, as well as better total accuracy compared to the broadside excitation.

2. The real and imaginary current error behaviors are more similar to each other (gradual minimization), whereas at broadside the real and imaginary current errors have unique behaviors (real error drops quickly with very few modes, while imaginary error is unchanged by most modes).

3. In all three conditions, the real current can achieve nearly perfect accuracy at broadside. When scanned far from broadside only the symmetric and positive definite case delivers acceptable accuracy.

While the modal sum behavior exhibits differences from broadside operation, we can safely say that if we make our impedance matrix symmetric and positive definite we can compose an accurate modal sum modal. Next we examine the modal far-fields directly, and plot the ones that correspond to the highest modal weighting coefficients. The H-plane normalized total far-field values of the driven solution and related modes are shown in Figure 3.13. In Case 1 and Case 2 we see that the driven field solution is largely characterized by two modal pairs, modes 3 & 4 and modes 5 & 6, respectively. The modal fields are clearly aligned along the main beam angle and

32
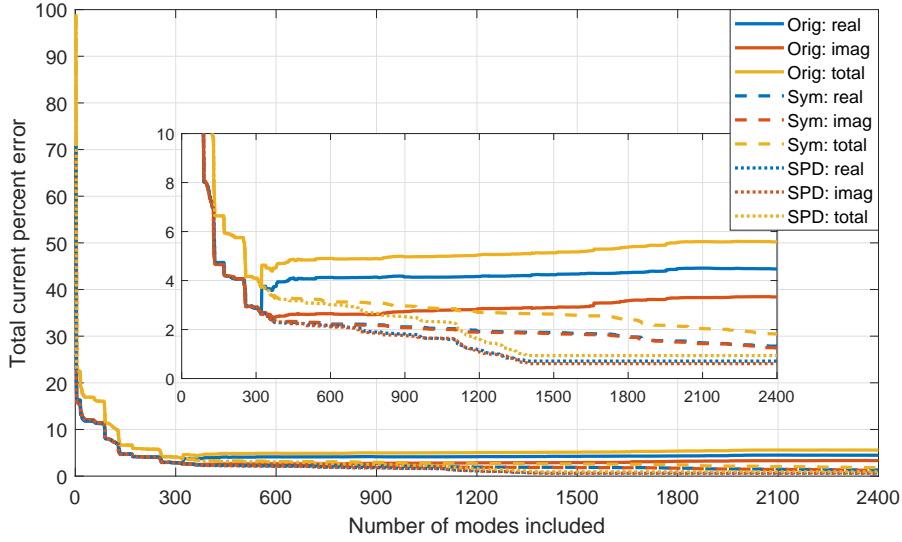
Figure 3.12: Total current percent error of a 40-element linear ring array ($d = 3\lambda/5$) with different impedance matrix conditioning. The array elements are excited with uniform amplitude and linear phase to steer the beam 41.8° from broadside.

also demonstrate major lobes along the grating lobe directions. Further, we note that lower order modes produce modal currents that exhibit spatial symmetry, and consequently modal far-fields that are symmetric along the E and H cut-planes. In Case 3 and Case 4 there are three highly weighted modes that largely align with the driven far-field. We note that these scan angles require the use of higher-order modes which result in modal-fields with multiple prominent lobes. The total field is therefore more reliant on the weighted interference between the modal far-fields, in order to produce a simple pattern of a single main lobe and single grating lobe. Due to the symmetric nature of the modal far-fields we note that if a modal pattern has a main beam at angle X and a grating lobe at angle Y, there will be mirrored lobes at angles $-X$ and $-Y$. Further we note that as the absolute difference between angles X and $-Y$ decreases, more modes are required in the modal summation, as seen in Cases 3 and 4. When that absolute difference is larger, as in Cases 1 and 2, we require fewer modes.
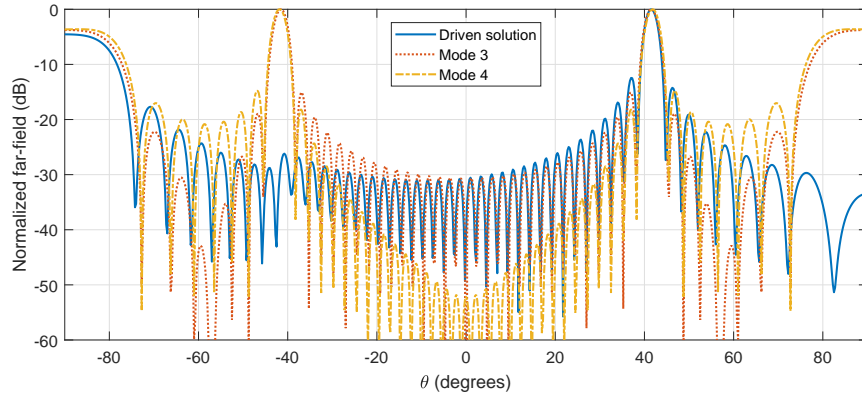
(a) Case 1: Scan angle +41.8°
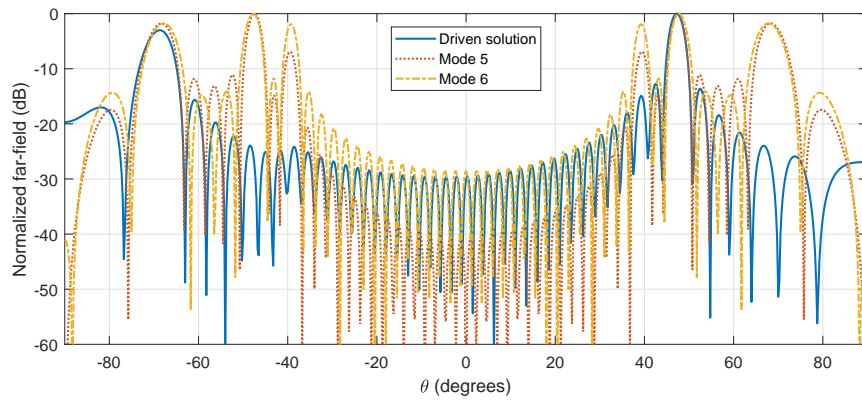
(b) Case 2: Scan angle +47.3°

Figure 3.13: Normalized total modal far-fields exhibiting main lobes corresponding to array scan angles and grating lobe angles.

34
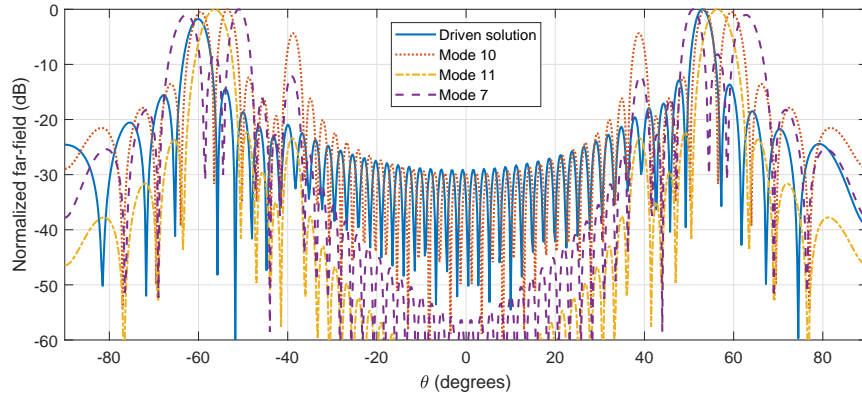
(c) Case 3: Scan angle $+53.1°$
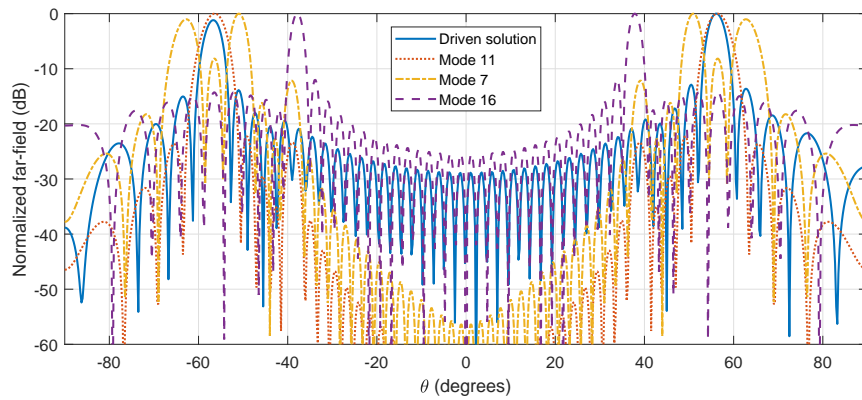
(d) Case 4: Scan angle $+56.2°$

Figure 3.13 (Continued): Normalized total modal far-fields exhibiting main lobes corresponding to array scan angles and grating lobe angles.

3.3 Chapter conclusions

Applying characteristic mode decomposition effectively requires meaningful accuracy metrics. In order to ensure we are solving for true characteristic modes we must ensure that our impedance matrices are properly conditioned, and we must understand the effects of impedance matrix variations on the CM eigenvalue problem. For resonant length rings we have shown how sensitive the CM problem is to fine dimensions and mesh density. Care must be taken when choosing a solver to generate the impedance matrix as small changes in how the EFIE problem is formulated can result in significant differences in achievable modal accuracy and the extent of reconditioning required. Expanding the problem space to very electrically large antenna arrays requires to us to solve larger problems and endure higher computational costs and decreased numerical accuracy in the eigenvalue problem solution stage. When operating a phased array we demonstrate how phase shifted excitations can cause meaningful variations in modal sum accuracy. While often treated as a plug-and-play methodology, we have shown that electrically large multi-port problems require extra care in their solution and eigenvalue decomposition stages.

CHAPTER 4

DIPOLE ARRAYS AND FINITE GROUND PLANES

In the previous chapter we studied large linear arrays of ring antenna elements and determined the modal accuracy behavior of the structure when operated as a phased array. We were able to determine modal far-fields that best characterized the array operation and connect the CM analysis to past works that utilized other decomposition methods. In this chapter we shift our focus to a different class of problem. For these simulations, we will be studying an array of half-wavelength dipoles over a finite rectangular ground plane, as shown in Figure 4.1. The inter-element spacing and the ground-plane separation are $\lambda/4$ at the frequency of interest. The dipoles are center-fed with delta-gap edge ports. This basic template design was chosen because we aim to identify modal properties and how they are related to individual common array features. This template design is simple in the hopes of allowing the effects to be separable from one another. Since the characteristic modes are dependent only on the geometry of the problem, due to the form of the CM eigenvalue problem Eq. (2.10), we note the most prominent structural properties of this template design:

- Electrically large ground-plane
- Half-wavelength dipoles
- Multiple ports
- Maximum dimension $\approx 2.23\lambda$
- Number of mesh edges ≈ 1100

and emphasize how these properties contrast with those of the typically electrically small structures analyzed with CM. Additionally, we note that the largest component in this design (the ground-plane) has no direct physical connection to any of the array elements and their feed points.
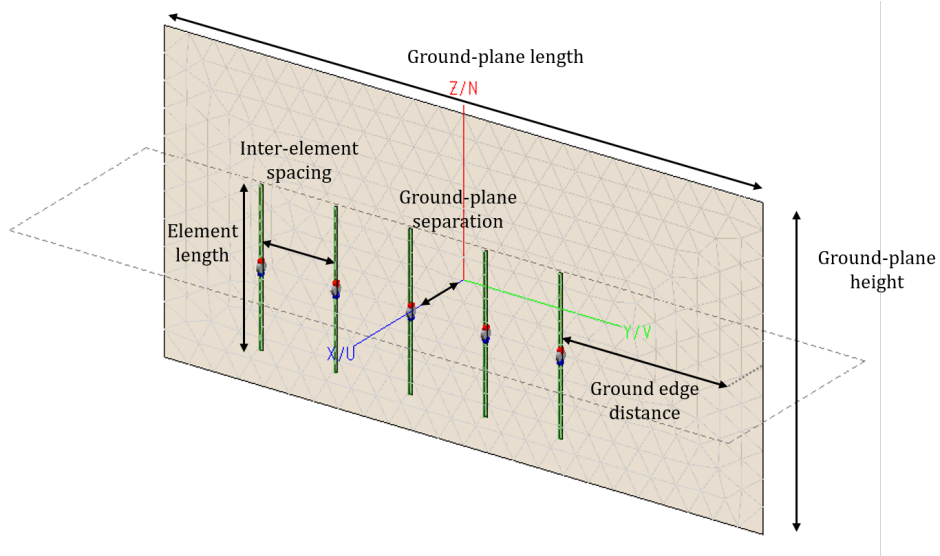
Figure 4.1: 3D model of the basic array template.

4.1 Ground-plane effects on modal accuracy

Comparing our basic template array from Figure 4.1 to the linear arrays of Chapter 3 we note that while the electrical size and structures are very different, both models have a similar number of discretized mesh edges. From a computational standpoint this will dictate the size of our impedance matrices. Therefore we expect that deviations in the modal behaviors of these arrays will be heavily driven by the presence of a finite ground plane. The new template array also uses half-wavelength dipoles as opposed to rings, but both are being used as resonant-type antennas that are electrically large. Our first test is on a basic array with five dipole elements, with $\lambda/4$ inter-element spacing. The rectangular ground-plane is $1\lambda \times 5\lambda/2$. For all simulations in this section we force the impedance matrix of our structure to be symmetric and positive definite. With this conditioned matrix we solve the CM eigenvalue problem and produce the complex modal weighting coefficients when the array is steered to broadside, with their magnitudes shown in Figure 4.2. The plot is truncated to the first 200 modes as there are no significant values with higher modal indices. We observe eight modes with relatively high weights, with these modes all being below modal index 30. However, while a few significantly weighted modes may be enough to capture the behavior of an electrically small radiator, after analyzing our 40-element array in the previous chapter, we anticipate the need for many more modes in order to
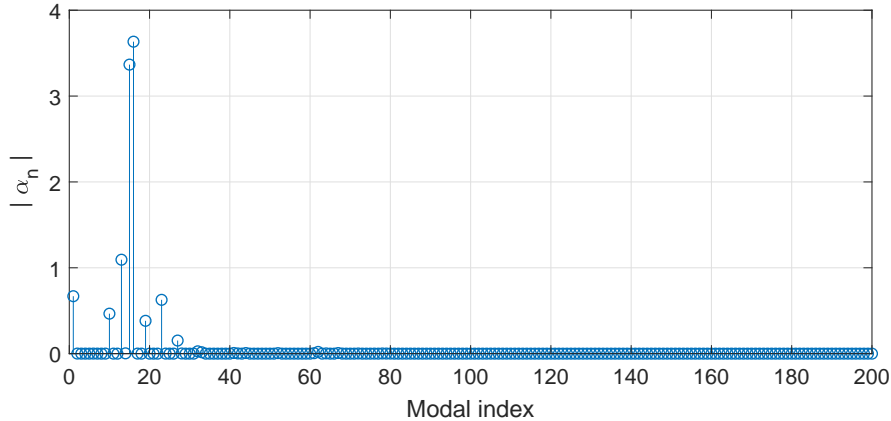
Figure 4.2: Magnitude of the modal weighting coefficients [Eq. (2.19)] of the basic array with five elements and $\lambda/4$ inter-element spacing steered to broadside.

compose an accurate modal sum.

Similar to the analysis of the linear array of rings, we calculate the total current percent error of our test array phased to radiate at broadside. The real and imaginary error components are shown in Figure 4.3, with two y-axes due to the large variation in scale between the results. We see that the current errors exhibit similar trends, notably that they both drop rapidly with the first sub-100 modes and do not experience another relatively major reduction until nearly mode 600. The results are plotted on a logarithmic scale to better show the effects of higher order mode inclusion, but we note that the real current error drops below 1% with as few as 23 modes. The same cannot be said for the imaginary current component which can only reach approximately 10% error once 600 modes have been included in the modal summation.

To determine if the presence of the ground plane has a pronounced effect on the scan accuracy of the modal sum, we calculate the total current percent error for a range of scan angles up 45°, as shown in Figures 4.4 and 4.5. The accuracy values for a complete modal sum are enumerated in Table 4.1. We observe that as scan angle increases the real current accuracy degrades, with the broadside excitation resulting in a perfect representation, ignoring the effects of numerical precision. The imaginary current however is most inaccurate at broadside, and over the range of samples beam angles never drop below 3% error. Notably the error minimization behavior is similar
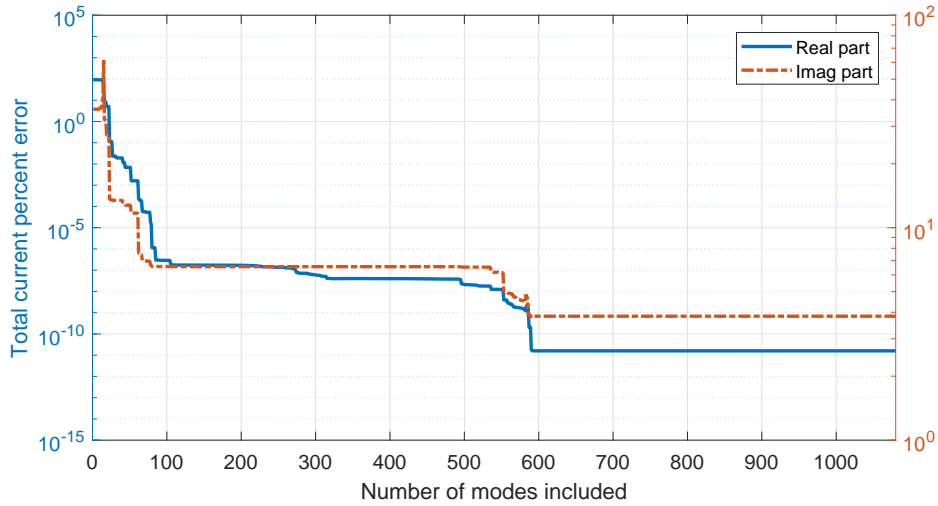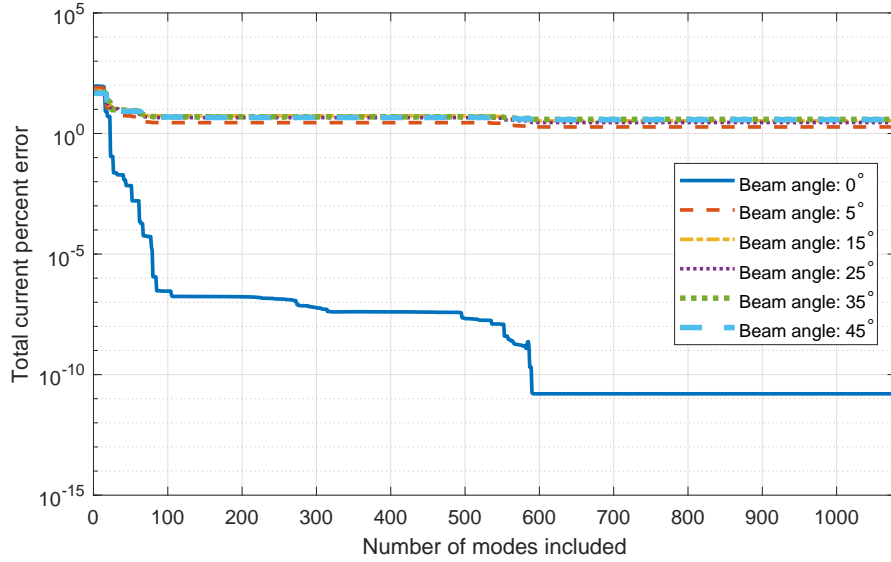
Figure 4.3: Comparison of the total current percent errors of the real and imaginary components for the five-element array with ground-plane, scanned to broadside.

Table 4.1: Total current percent error values for a complete modal summation of the five-element array with ground-plane for a range of scan angles.

Scan Angle	Real **J** Error	Imaginary **J** Error
0°	1.598e-11	3.831
5°	1.867	3.407
15°	3.340	2.632
25°	2.853	3.771
35°	3.862	3.204
45°	3.747	3.237

across the range of beam angles as a qualitative matter, but differs in the range of achievable error values.

Examining the far-field percent error as presented in Figure 4.6, we note that at all of the test beam angles we can achieve less than 1% error with as few as 35 modes included. Compared to the peak current accuracy values in Table 4.1, we see that a structure with a large ground-plane can produce a very accurate modal far-field summation for a range of excitations, while the modal current error may still be unacceptable for certain analyses.

Figure 4.4: Total current percent error of the real current component for the five-element array with ground-plane, scanned from broadside to 45°.
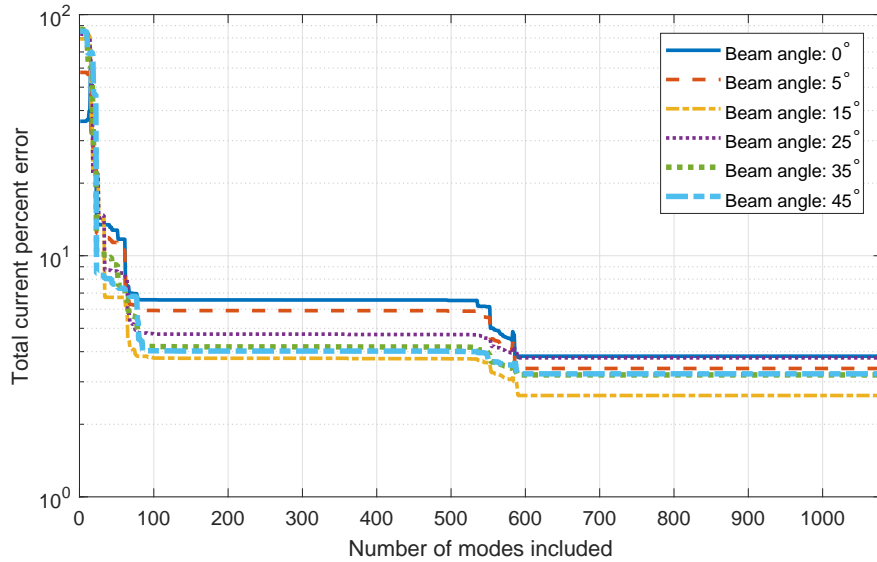
Figure 4.5: Total current percent error of the imaginary current component for the five-element array with ground-plane, scanned from broadside to 45°.
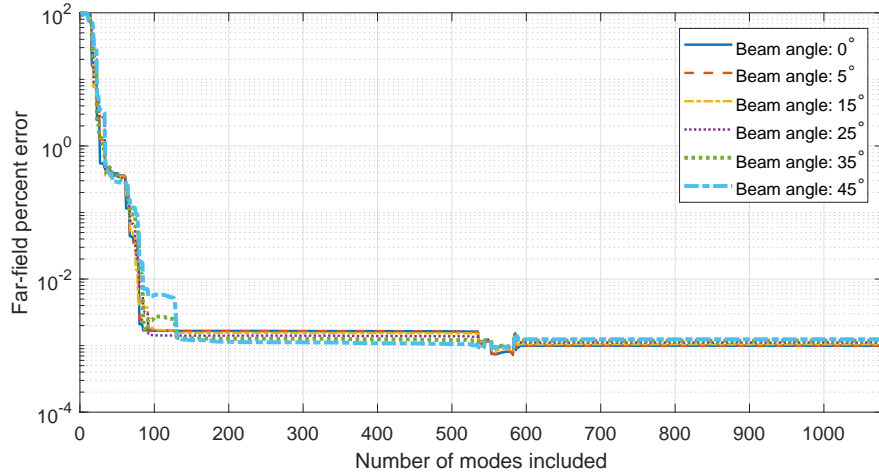
(a) Far-field percent error on a logarithmic scale.
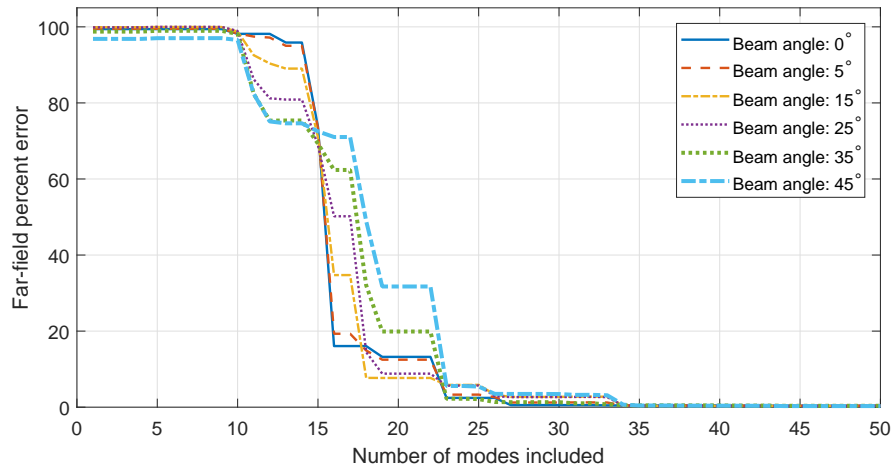
(b) A close-up view of the far-field percent error of the first 50 modes on linear scale.

Figure 4.6: Far-field percent error [Eq. (3.9)] for the five-element array with ground-plane, scanned from broadside to 45°.

Table 4.2: Properties of the four test arrays used for the fixed aperture study. All electrical lengths are relative to $f_0 = 100$ MHz where the array elements are $\lambda/2$ long.

Number of elements	Inter-element spacing	Free-space isotropic directivity
3	λ	3
5	$\lambda/2$	5
7	$\lambda/3$	4.803
9	$\lambda/4$	4.728

4.2 Array inter-element spacing effects

4.2.1 Fixed aperture arrays

With the basic design illustrated in Figure 4.1 in mind, we approach a common problem faced in array installations. If a user requires a certain amount of gain from an array but is limited by platform size, how can they best utilize the fixed aperture? Does it benefit the user to increase the number of elements with smaller inter-element spacing, or to have a more sparsely spread array of fewer elements? As a practical application matter, if an array has fewer elements, each element must handle more power in order to maintain an acceptable total radiated power. To study and compare the performance trade-offs we simulate four arrays of half-wavelength dipoles, with element spacing shown in Table 4.2. For all four arrays we fix the ground-plane size as $\lambda \times 2.5\lambda$, and place the ground-plane $\lambda/4$ behind the array. As labeled in Figure 4.1, this leaves a ground-edge distance of $\lambda/4$ between the outermost elements and the ground-plane edge. We note that this distance is with respect to the $\hat{y}$ dimension.

In order to demonstrate the type of performance trade-off we should anticipate from our full-wave simulations we initially calculate the directivity of a simplified scenario. For a uniformly excited, equally spaced linear array of isotropic sources in free-space, the directivity is formulated following [29]:

$$D = \frac{\left| \frac{\sin(N\delta/2)}{N\sin(\delta/2)} \right|^2}{\frac{1}{N} + \frac{2}{N^2} \sum_{m=1}^{N-1} \frac{N-m}{m\beta d} \sin(m\beta d) \cos(m\alpha)} \tag{4.1}$$
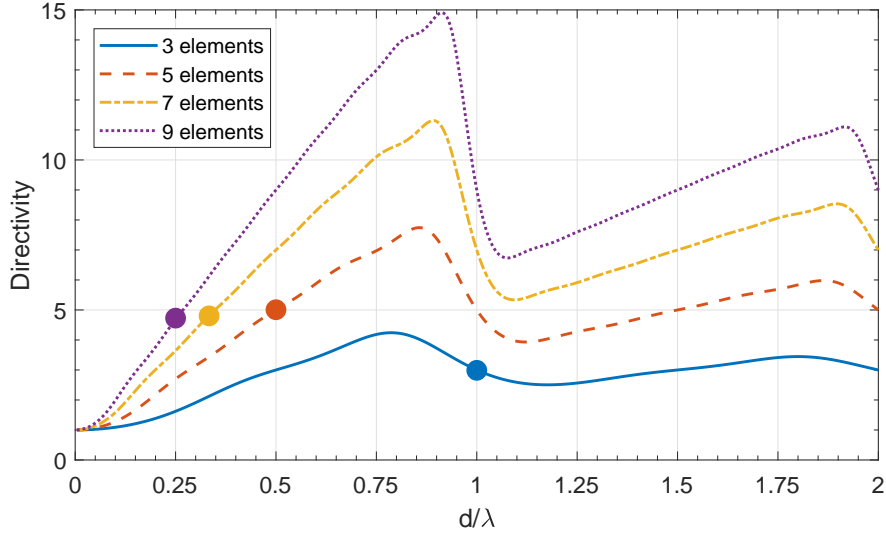
Figure 4.7: Directivity of a uniformly excited, equally spaced linear array [Eq. (4.1)] for fixed length arrays with variable numbers of elements. The circular markers indicate the electrical spacing values at $f_0 = 100$ MHz.

where N is the number of elements, d is the inter-element spacing, β is the wavenumber, α is the inter-element phase difference, and δ is any phasing beyond that used for ordinary endfire operation. For a range of inter-element spacing values we calculate D for a broadside excitation, as shown in Figure 4.7. The bold points mark the noted free-space isotropic diversity values shown in Table 4.2. We note that this formulation does not include the effects of mutual coupling between elements or any specific element factors. As N increases we see that the fixed aperture constraint, which forces the inter-element spacing to decrease, appears to limit the achievable directivity.

Next, we simulate our four array configurations using the FEKO MoM solver, now including a finite ground-plane. Solving for the far-fields, and feeding the array elements each with a $Z_0 = 50\Omega$ transmission line model, we calculate the realized gain for the array with a ground-plane. The results at broadside are shown in Figure 4.8 over a frequency range where the length of a single dipole l varies from 0.4λ to 0.55λ. Additionally we simulate the array without a ground-plane, as shown in Figure 4.9, noting that the full-wave simulation does account for mutual coupling. Operating at the frequency that makes the array elements half-wavelength dipoles ($l/\lambda = 0.5$) we see that the full-wave results, with and without ground-planes, follow the directivity trends indicated by the simplified formula [Eq. (4.1)]. Most
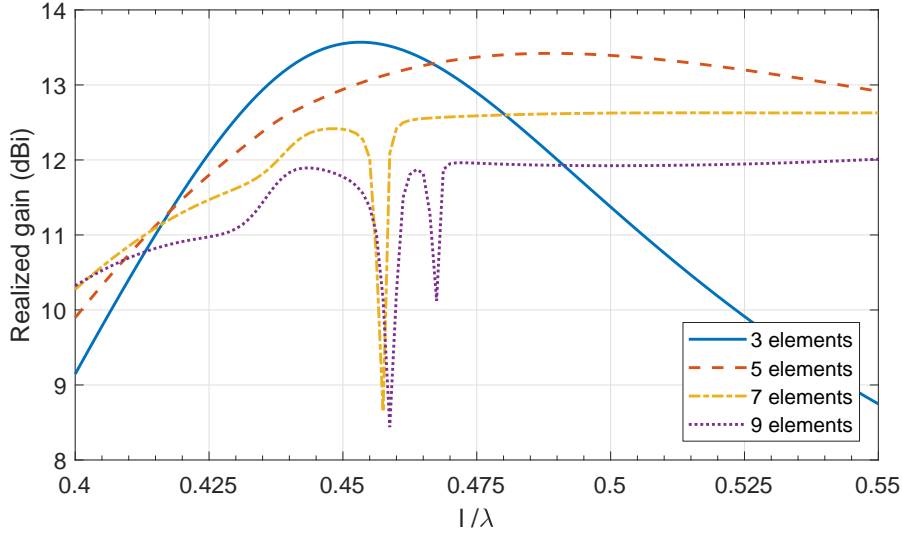
Figure 4.8: Realized broadside gain values for four fixed aperture arrays with a finite ground-plane.

Table 4.3: Electrical length of inter-element spacing at the frequencies where realized gain drops dramatically, as shown in Figures 4.8 and 4.9.

Number of elements	Spacing (no ground)	Spacing (with ground)
7 dipoles	0.2225λ	0.2288λ
9 dipoles	0.2228λ 0.2331λ	0.2294λ 0.2338λ

notably we observe significant drops in realized gain for the arrays with 7 and 9 elements when the elements are at sub-resonant lengths, both with and without a ground-plane present. This indicates that the effect is largely driven by mutual coupling due to the inter-element spacing values, and not the presence of a ground-plane. In Table 4.3 we note the electrical length of the inter-element spacing at the frequencies where the realized gain decreases most.

4.2.2 Error due to inter-element coupling

Having observed a strong coupling effect from the fixed-aperture arrays, we simulate a five-element array in free-space for a range of inter-element spacing values with a broadside excitation. We then calculate the total current
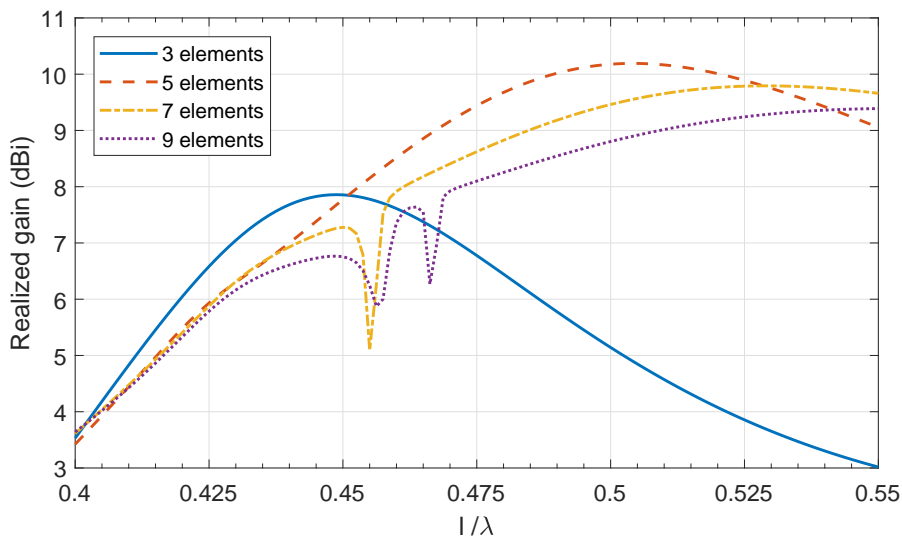
Figure 4.9: Realized broadside gain values for four fixed aperture arrays in free-space.

percent error to determine if the coupling behavior in these cases can be well represented by a sum of characteristic mode eigencurrents. The real and imaginary current error values are shown in Figure 4.10, with two different y-axes due to the large variation in error values. We draw the following insights from the results:

1. For a broadside excitation the real current error is effectively negligible for a wide range of inter-element distances, including very tightly coupled elements.

2. The imaginary current error peaks when the elements are approximately $\lambda/2$ apart, and in general is higher when the elements are tightly coupled. Therefore the imaginary current distributions that are induced by a tightly coupled array are poorly represented by the characteristic mode set of eigencurrents.

Array resonance and radiated power

In addition to observing the drop-off in broadside radiation, we can examine the port impedance values of our five-element array in free space as well. Figure 4.11 shows the port resistance and reactance values for elements 1

46
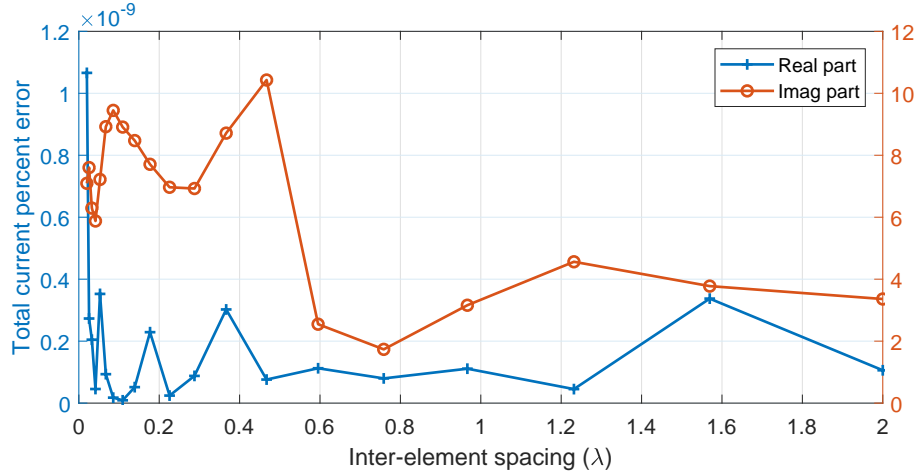
Figure 4.10: Total current percent error of a five half-wavelength dipole array with variable inter-element spacing.

through 3, where element 1 is the outer-most element, and element 3 is the center element. Due to the symmetric nature of the excitation, impedance values for elements 4 and 5 are not shown. We note that the drop in realized gain coincides with all the port impedance values rapidly approaching zero, as a function of frequency. This effect is commonly seen when one encounters a blind-angle for a phased-array. At that particular scan-angle inter-element interference results in zero port impedance, and a drop in radiated power. It is particularly interesting to observe this effect when the array is excited for broadside radiation, making this effect more of a "blind frequency."

To explore this effect further we expand the array, making a nine-element dipole array. Element length and spacing are preserved from the previous example. Figure 4.12 shows the real and imaginary port impedance values at broadside. Adding these four additional elements clearly changes the array behavior, but the "blind frequency" effect is essentially preserved, with very large variations in resistance and reactance seen below the element resonance point. As shown in Figure 4.13, these variations align with two severe drops in radiation efficiency for the entire array. In this example a total power of 1 Watt is incident across all ports and the loss of efficiency is due to impedance mismatch at the element ports. Examining this efficiency plot we determine three frequency points of interest: the two "dip" frequencies where efficiency drops, and the frequency where efficiency is highest. The current percent error values at these points are shown in Figures 4.14 and 4.15. Table 4.4
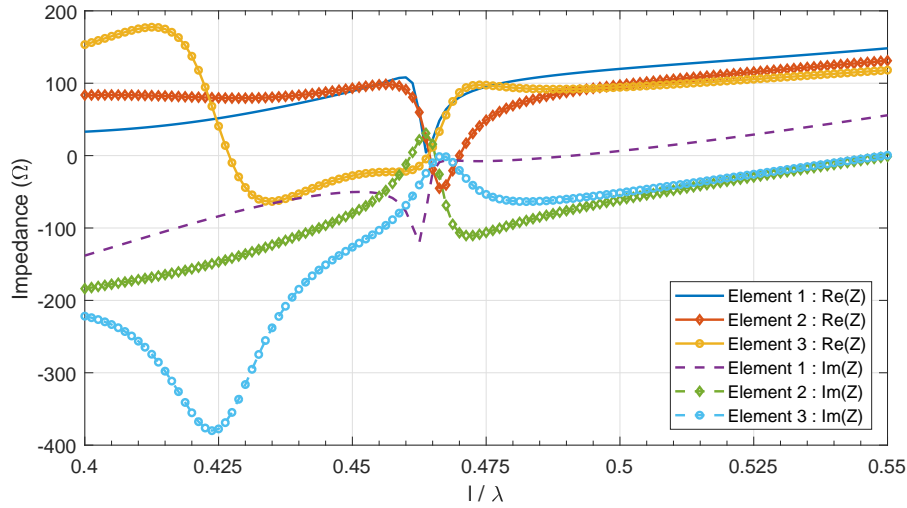
47

Figure 4.11: Port impedance values of a five half-wavelength dipole array with $\lambda/4$ inter-element spacing, over a range of frequencies, radiating at broadside.

Table 4.4: Data points from Figures 4.14 and 4.15, cataloging the minimum number of modes needed to achieve a certain percent error. Table entries depict the error of the current magnitude / the error of the real part of the current. The omitted value indicates that the desired percent error is unachievable.

Percent error	First dip	Second dip	Peak radiation
$< 10\%$	7/5	7/6	9/5
$< 5\%$	7/5	7/6	17/5
$< 2\%$	18/7	7/7	71/5
$< 1\%$	64/7	20/7	—/5

presents the number of modes needed to attain a desired percent error, both in terms of total current error, and real part. Entries for the imaginary parts are omitted because in most cases the real part of an error is incredibly low, making the total error value almost entirely dependent on the imaginary error component.

In Figure 4.16 we compare the magnitude of the modal weights at the three frequencies of interest. Relative to one another, there are no significant modal weights beyond mode 10. We note that these results are from three independent simulations, with the modal indices determined by the characteristic mode eigenvalue magnitudes at each frequency. Therefore "mode x"
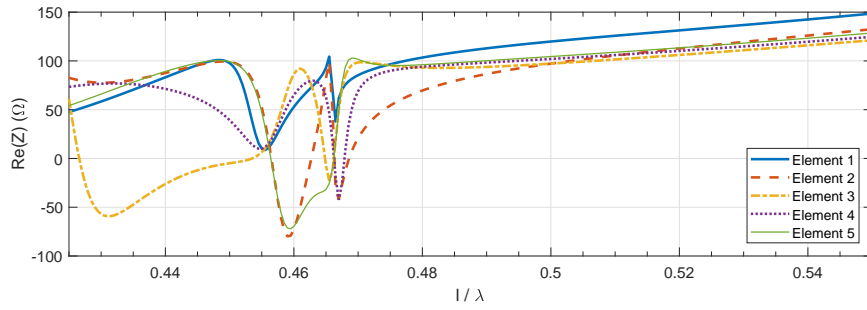
(a) Error at $l/\lambda = 0.4570$
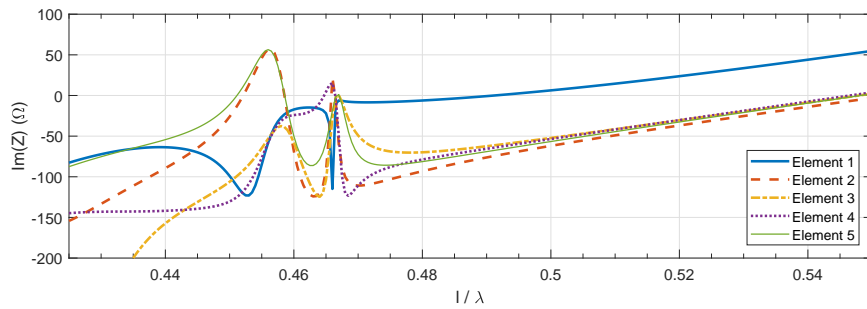
(b) Error at $l/\lambda = 0.4665$

Figure 4.12: Total current percent error values of a nine-element array of strip dipoles at the two frequencies where the array exhibits dips in total radiated power.
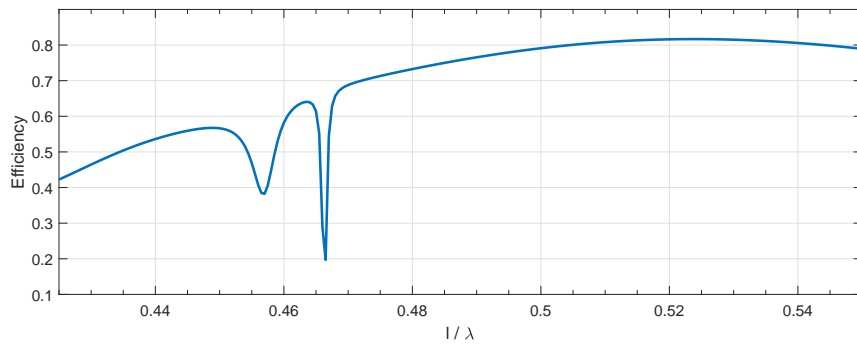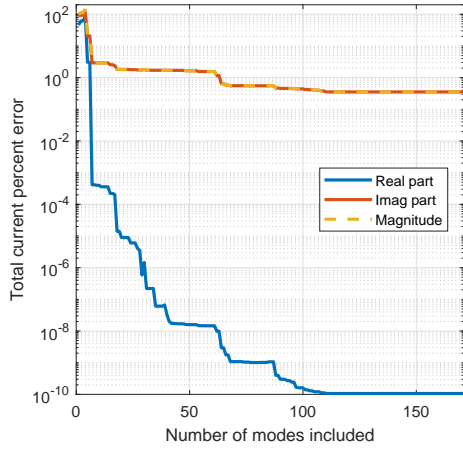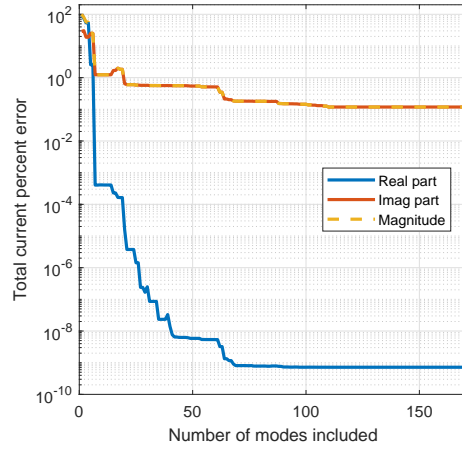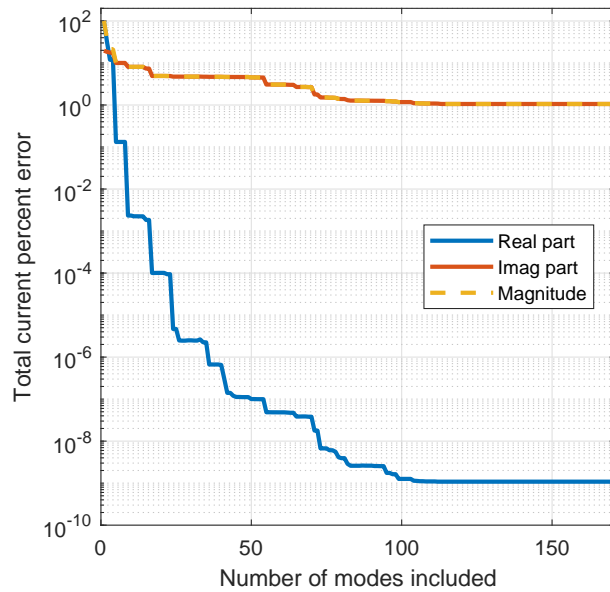

Figure 4.13: Radiation efficiency of a nine-element array of strip dipoles.

(a) Error at $l/\lambda = 0.4570$.

(b) Error at $l/\lambda = 0.4665$.

Figure 4.14: Total current percent error values of a nine-element array of strip dipoles at the two frequencies where the array exhibits dips in total radiated power.

Figure 4.15: Total current percent error values of a nine-element array of strip dipoles at $l/\lambda = 0.5240$, where the array radiates the peak amount of power.

at the first frequency of interest may not be related in any way to "mode x" at the second frequency point. In order to make a meaningful comparison and observe how a mode changes between these frequencies we must use a mode tracking algorithm, as described in Section 2.4. Figures 4.17 and 4.18 show the tracked eigenvalue traces for the first 15 modes. In each figure a vertical dashed line indicates the frequency modes are tracked from. This means that the algorithm attempts to track what are designated as the 15 most significant modes at that frequency, and that those modes may not be modally significant at all frequencies.

Examining the results we can observe a number of difficulties the tracking algorithm experiences. The most obvious problem is that in some cases the algorithm loses track of a mode, which results in a truncated eigenvalue trace. This problem is evident in all three examples. It is caused by the algorithm failing to find a suitable match between the mode in question and all of the modes at an adjacent frequency point. Numerically this means the inner products of these modes are all below a reasonable threshold, indicating that there is no correlation between the modes. This problem may arise due to inadequate frequency sampling, even in electrically small problems where eigenmodes typically change very slowly with frequency. The presented results are made with 251 frequency points, with increments of 100 kHz over the range of 85 MHz to 110 MHz. Finer frequency sampling did not produce markedly better results and in practice is very computationally expensive, requiring a new impedance matrix to be formulated and eigenvalue problem solved at each added frequency point. In all three examples one can also observe a number of eigenvalue crossing avoidances. Previous work has explored this issue [30], which manifests as pairs of eigenvalue traces that, instead of crossing as they approach each other, diverge and "switch" paths. Past work has shown that these pairs of modes can sometimes be decoupled resulting in a more gradually changing eigenvalue path as well as more consistent eigenvector designations. Our array problem is particularly prone to this problem as shown by the multiple crossing avoidances that appear in even the first ten most significant modes. This is problematic since the utility of multi-frequency studies is dependent on how well modal behavior can be tracked over the frequency range in question. Characteristic modes for this scale of problem struggle with multiple issues making it very difficult even to consistently define modes over a wide bandwidth. Alternative track-
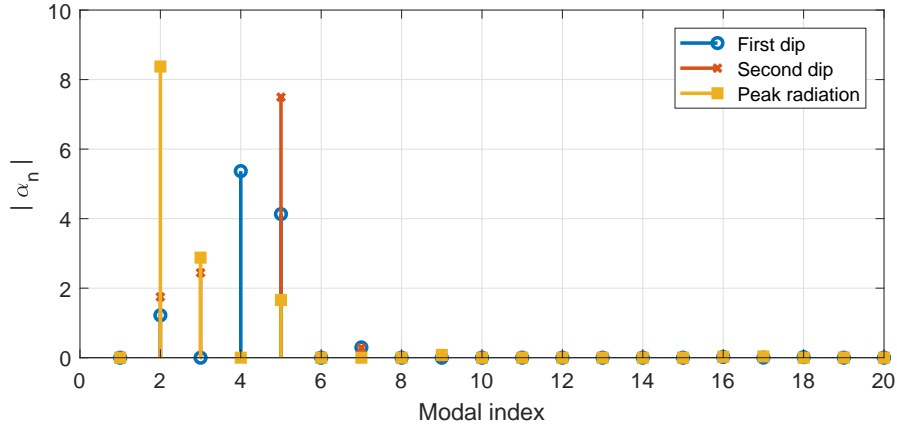
51

Figure 4.16: Modal weight coefficients of a nine-element array of strip dipoles driven at broadside at three frequency points.

ing methods rely on tracking the modal far-fields of the eigencurrents [31]; however, attempts to implement it on this scale of problem yielded similarly poor results. Hybrid tracking methods are a necessity in these cases and are a growing area of research.

4.3 Ground-plane effects

4.3.1 Array and ground-plane mode differentiation

In all of our modal summations so far, when calculating our error metrics we ordered our characteristic modes according to their eigenvalue magnitude, as is often the convention in CM analysis. Adding an additional means of classifying modes, we visually examined the modal eigencurrent magnitudes of the first 50 modes of our template, and labeled them either "array modes," "ground modes," or "interaction modes." This simple classification was determined by the peak eigencurrent values and whether they were primarily located on the array structure, ground-plane, or some combination of the two. Examples of the most distinct currents, which we refer to as "locally dominant" currents, are shown in Figure 4.19. Of the first 50, only four modes were deemed interaction modes. As shown in Figure 4.20, we define an interaction mode as one that exhibits spatial variance that is dependent on the dimensions of both the array and ground-plane. Stated differently,
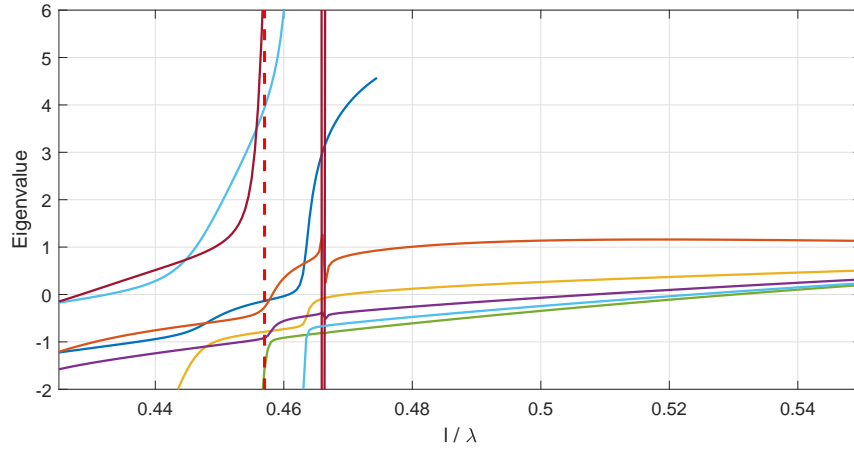
(a) Mode tracking started from $l/\lambda = 0.4570$
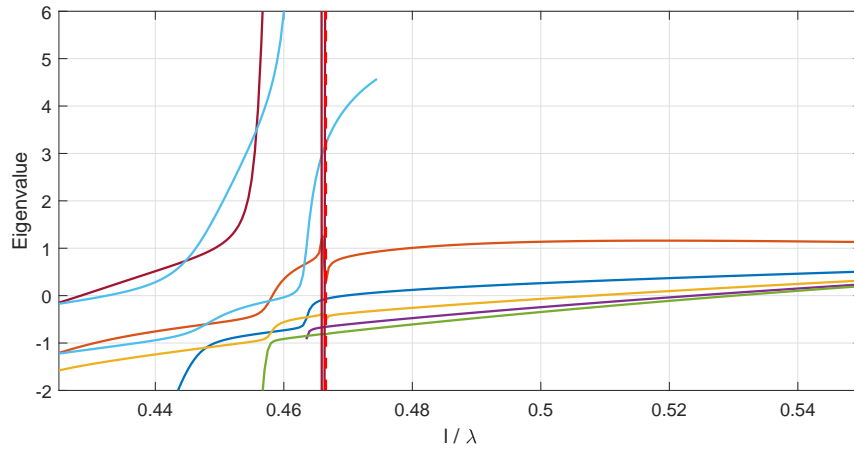
(b) Mode tracking started from $l/\lambda = 0.4665$

Figure 4.17: Tracked modal eigenvalues of a nine-element array of strip dipoles with the modal tracking algorithms started at the "dip" frequencies, as indicated by the vertical dashed lines.
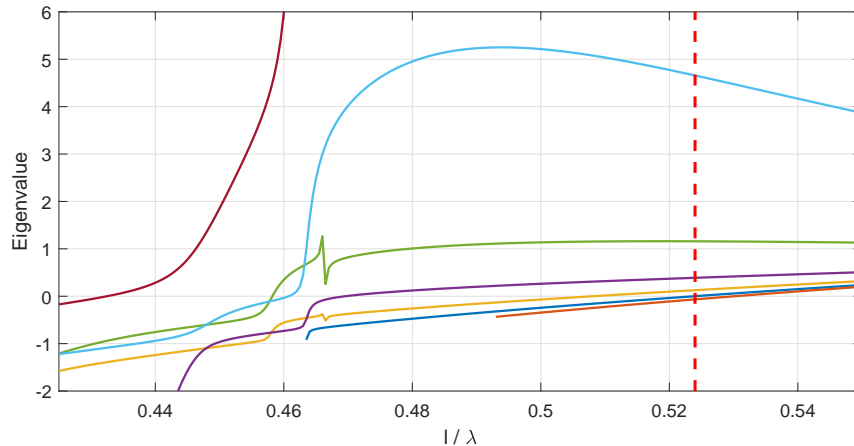
Figure 4.18: Tracked modal eigenvalues of a nine-element array of strip dipoles with mode tracking started from $l/\lambda = 0.5240$, as indicated by the vertical dashed line.

an interaction mode current distribution is one that cannot be entirely attributed to either the array or ground-plane geometry. While we know a driven solution of our test array will yield a main beam at broadside and minimal radiation in the backplane due to the presence of our ground-plane, we note that the modal far-fields of our structure are indifferent to how the structure is fed. As shown in Figure 4.21, whether we examine the modal far-field of an array, ground, or interaction mode, all of them produce symmetric patterns in the H-plane; it is only through the complex summation that the modal fields produce anything resembling the radiation pattern of our array with a ground-plane. This differs from the array in free-space examined in Chapter 2 where in many cases a single modal far-field largely encompassed the behavior of the driven radiation pattern.

Since we drive our structure through ports located on the array elements, we decide to examine whether sorting our modes in order of their array dominance would result in a more rapid error minimization. We determine a new ordering by sampling the weighted modal eigencurrents at the array ports, and ordering our modes from highest to lowest magnitude average port current. We compare the total current percent error trends of this ordering and the traditional eigenvalue magnitude ordering in Figure 4.22. Unexpectedly, we see that the new ordering actually slows the error minimization of the real current component, moving the "needed" modes to higher indices. Conversely, the imaginary current component is minimized much more rapidly.
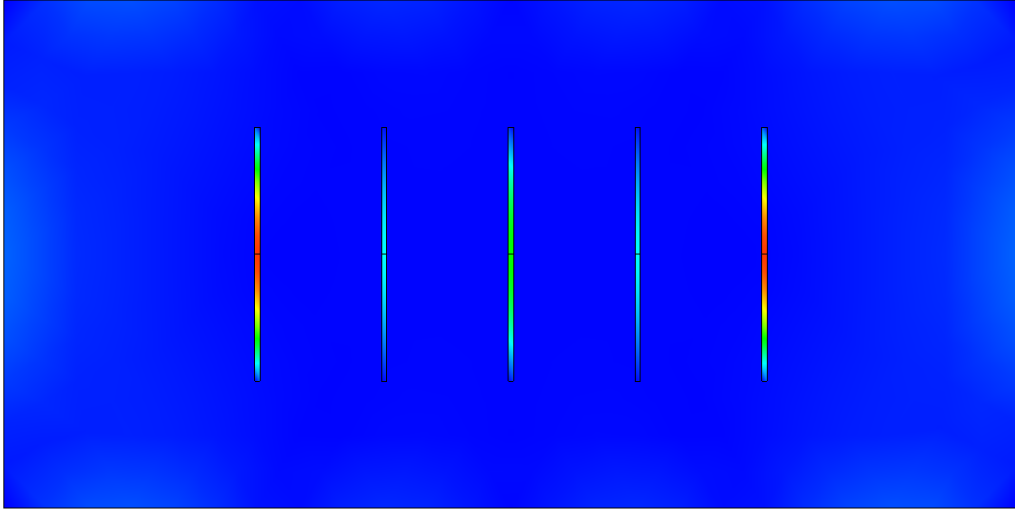
(a) Array dominated eigencurrent: mode 1
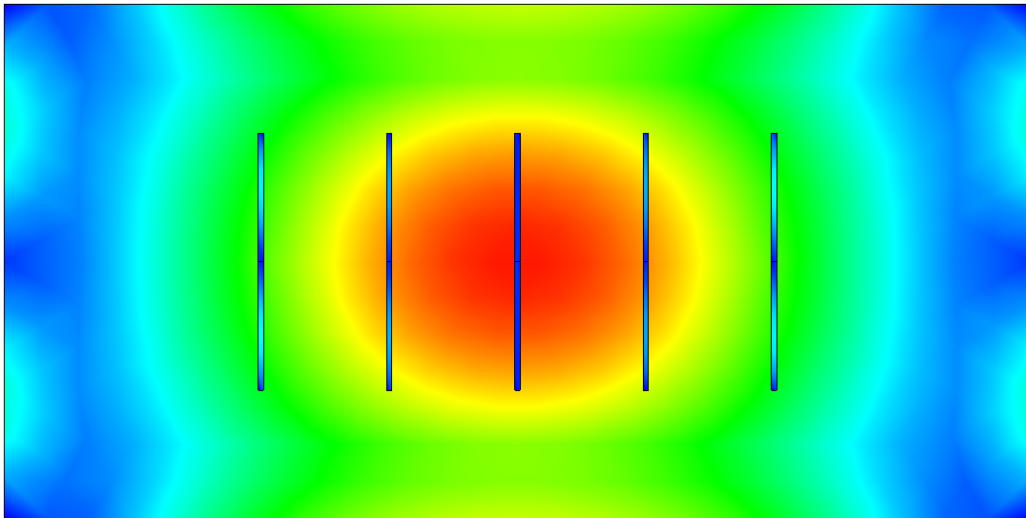
(b) Ground-plane dominated eigencurrent: mode 2

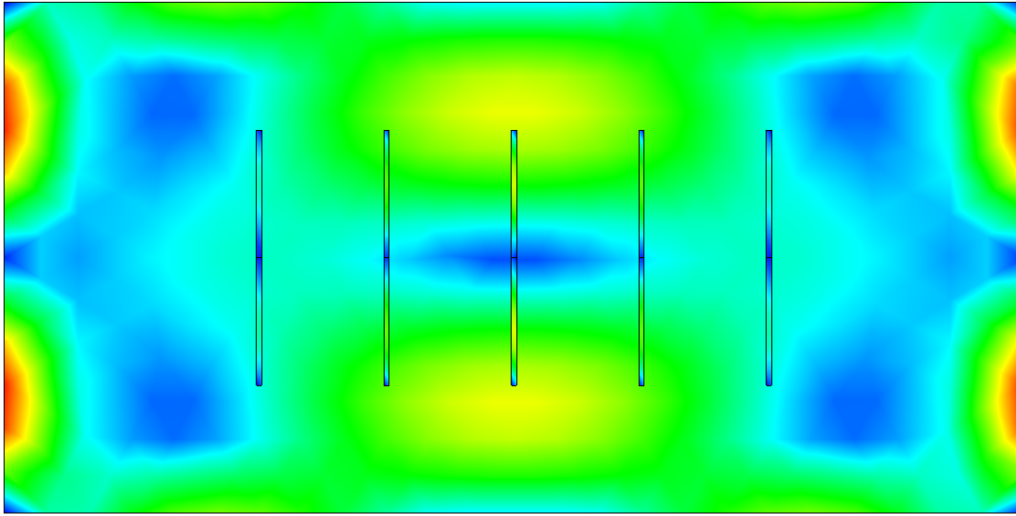Figure 4.19: Eigencurrent magnitudes of locally dominant type modes.

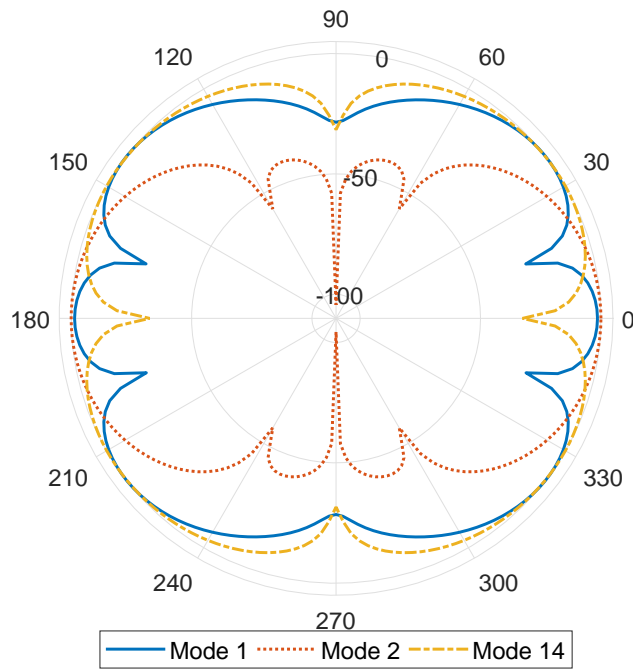Figure 4.20: Magnitude of interaction eigencurrent: mode 14.

Figure 4.21: Normalized H-plane modal far-fields of the eigencurrents shown in Figures 4.19 and 4.20.
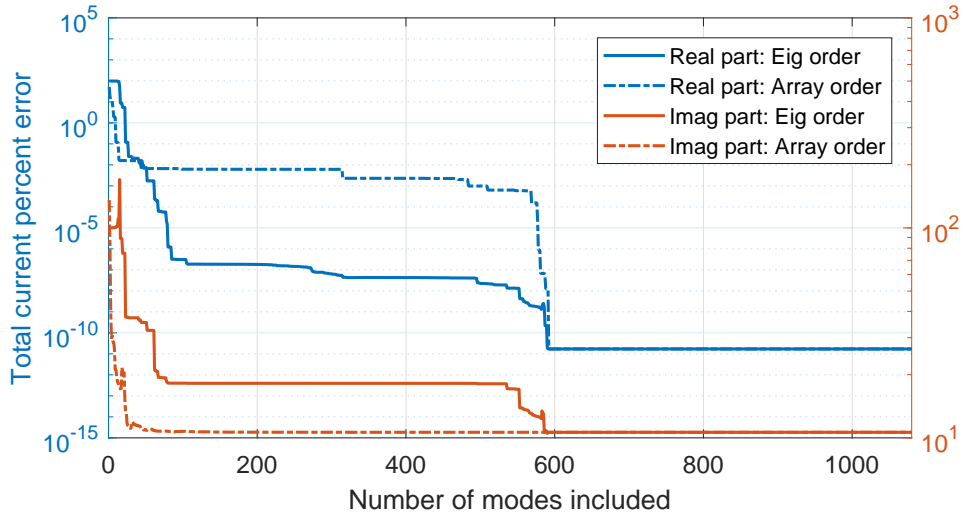
Figure 4.22: Total current percent error of a broadside array excitation with different modal orderings.

As expected, the values converge past a point, as we were simply changing the ordering of a linear summation. Additionally we inspect the far-field percent error of this alternative ordering, with the results shown in Figure 4.23. For most of the summation the array based ordering more rapidly minimizes the CM modal far-field error, with 48 modes needed to achieve 1% error in the array ordering, as compared to 67 modes with eigenvalue based ordering.

4.3.2 Complex modal weights and beam-steering

In the previous section we demonstrated how array dominant modes tend to have a more significant impact on the accuracy of a modal summation. In addition to a typical broadside excitation, we wonder then how the modes relate to one another as the array is phase shifted. In the CM modal summation of Eq. (2.16) we can isolate the weighting factor α and plot its change in magnitude and phase as a function of beam angle change. Figure 4.24 presents what we refer to as the delta-weights of a five-element half-wavelength dipole array above a rectangular ground plane, as depicted in Figure 4.1. Applying a uniform phase progression and equal amplitude excitation we steer the beam angle in 1° increments and plot the change in modal weight magnitude and angle. The angle values are wrapped such that they all lie between +180° and −180°. The color of the data points varies
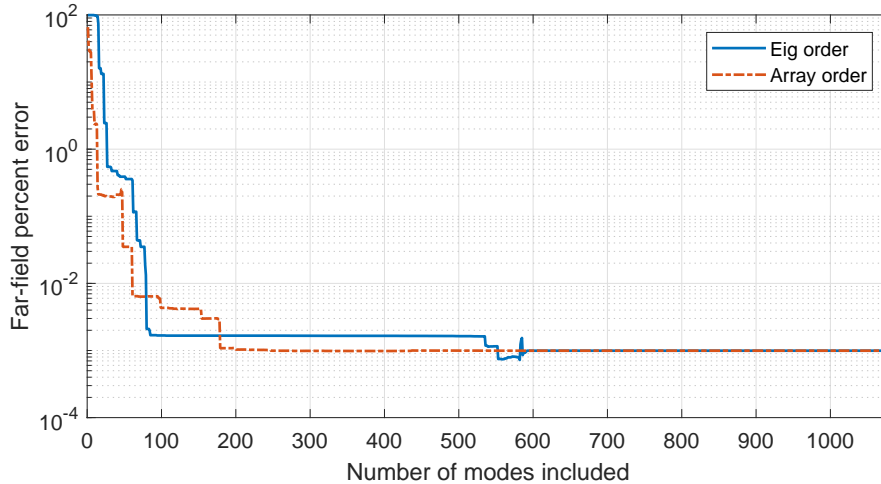
Figure 4.23: Far-field percent error of a broadside array excitation with different modal orderings.

from magenta, indicating high weighted average current at array ports, to cyan, indicating low current. The color scale is dictated by a uniform scale based on the ordering of port current magnitude among the first 50 modes, as designated by traditional eigenvalue based ordering. Figure 4.25 presents the same type of data for the array but with 5° beam angle increments.

Immediately two trends become evident. First, array dominant modes (magenta points) undergo a range of magnitude changes; however, they all experience the same change in angle. This is evident in the magenta points being spaced in horizontal lines. Second, the ground-plane dominant modes (cyan points) demonstrate no significant change in magnitude, but a range of differences in angle. This is evident in the cyan points being spaced in vertical lines. We observe that the array modes mostly fall into a single horizontal span, with occasional outliers. The delta values of the first increment from broadside deviate the most from these trends. This is consistent with our previous results that show strong variation in the modal sum as soon as the symmetric current of a broadside excitation is perturbed. The delta weight angle value of this horizontal group is dependent upon the beam steering increment, with the observed values cataloged in Table 4.5. We note that the delta weight value tends to decrease the further the beam is steered from broadside, as indicated in the third column of the table. The clear divide in modal behavior between array and ground dominant modes provides an eigenvalue based method of determining a mode's geometric properties

Table 4.5: The change in the complex weight angle of array dominant modes for a range of beam-steer increments and beam angle ranges. Plots for scan increments of 1° and 5° are shown in Figures 4.24 and 4.25. The remaining plots are shown in Appendix B.

Scan increment	Beam angle range	Array Δ weight angle
1°	0° to 9°	−4.9° to −4.6°
2°	0° to 18°	−9.4° to −8.2°
3°	0° to 27°	−14.1° to −12.7°
4°	0° to 36°	−18.7° to −14.9°
5°	0° to 45°	−23.3° to −17.3°

without having to view the eigencurrent distribution directly. This could serve as a classifier in modal data processing methods.

4.3.3   Ground-plane as loading element

An emerging approach to analyzing arrays with characteristic mode analysis consists of viewing the total structure as a composition of sub-structures [32]. For our template dipole array we divide the design into the array elements and the finite ground plane. As we have seen before, when solving the original characteristic mode problem for the entire structure, we arrive at solutions that feature ground plane current dominated modes. However, often the solved eigencurrents are used in order to determine the input impedance at potential feed points on a structure. As we never intend on feeding the overall structure from the finite ground plane, this results in a solution featuring large amounts of eigenvector data that are not necessarily of major importance. Without any modification, our original problem takes the form

$$
\begin{aligned}
[Z_{AA}]\,[J_A] + [Z_{AB}]\,[J_B] = [V_A] \\
[Z_{BA}]\,[J_A] + [Z_{BB}]\,[J_B] = [V_B]
\end{aligned}
\tag{4.2}
$$

where the subscript A represents the antenna array, and the subscript B represents the ground plane. J and V represent the current and voltage values that are either observed or impressed, respectively. Since we know we will not be feeding the structure through the ground plane, we can safely set
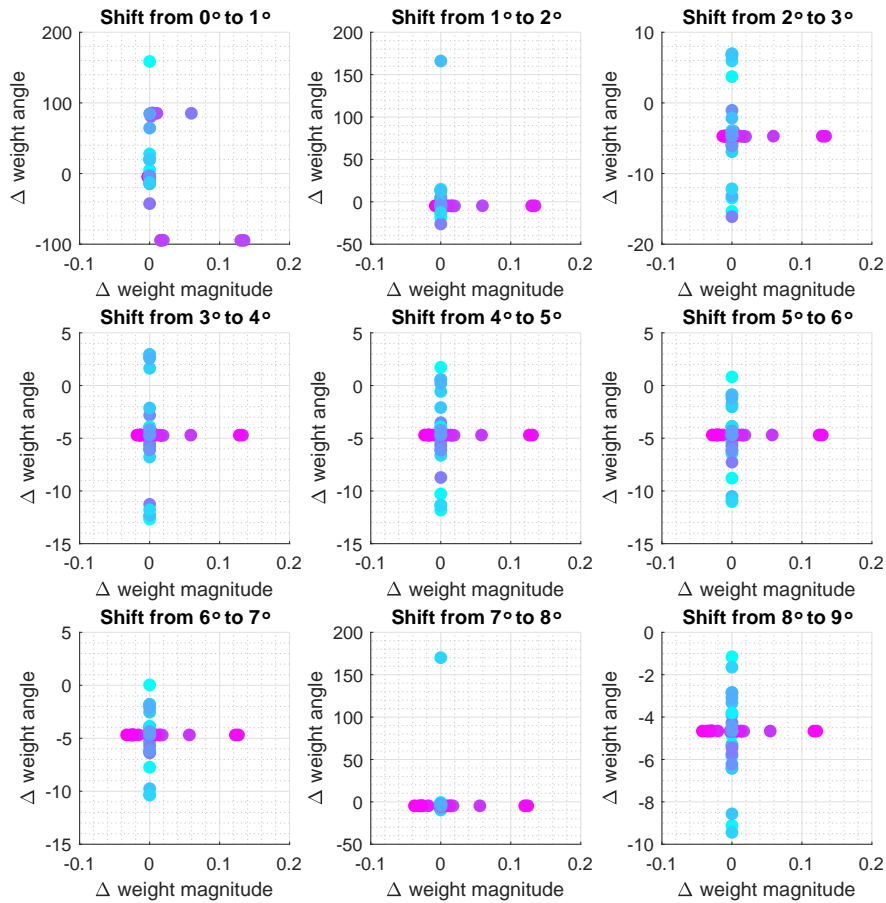
Figure 4.24: Delta weight values for a five-element dipole array above a rectangular ground-plane with beam scanned in 1° increments from broadside. The color scale from cyan to magenta indicates the average modal current magnitude at the array ports, ranging from low density (ground-modes) to high density (array-modes).
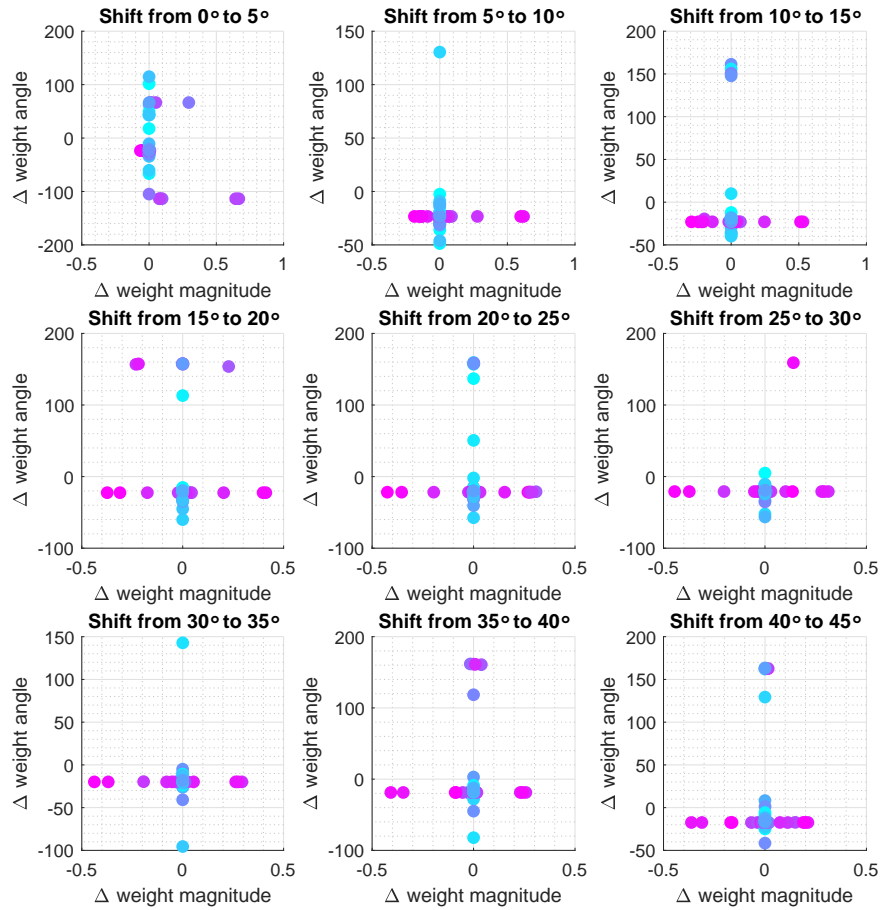
Figure 4.25: Delta weight values for a five-element dipole array above a rectangular ground-plane with beam scanned in 5° increments from broadside.

V_B to zero. Some algebraic manipulation lets us then define V_A as

$$\left\{ [Z_{AA}] - [Z_{AB}] [Z_{BB}]^{-1} [Z_{BA}] \right\} [J_A] = [Z_{SUB}] [J_A] = [V_A] \qquad (4.3)$$

where Z_{SUB} now includes the self-matrix of the antenna array as well as the loading effect of the ground plane. If we need to solve for the equivalent eigencurrents on the ground plane we can easily calculate them as

$$[J_B] = - [Z_{BB}]^{-1} [Z_{BA}] [J_A] . \qquad (4.4)$$

If we rebuild our total modal current sum using Eqs. (4.3) and (4.4) we can concatenate the resulting current vectors and compare their accuracy to a direct MoM solution. Figure 4.26 shows the percent current error values as a function of edge index. Values to the left of the vertical red line are the edges of the array elements. The values to the right of the vertical red line are the many edges on the finite ground-plane. We can see that the ground-plane current error is dominant, while the array element current is in alignment with the MoM solution. Directly comparing the results we plot the current percent error as a function of modes added to the modal sum, as shown in Figure 4.27. We observe that the error introduced by the substructure approach has no appreciable effect on the imaginary current accuracy. However, it is clear that the substructure method limits the accuracy of the higher-order real currents. While substructure decomposition is attractive for problems where large portions of the design are unchanged or not directly excited, these results show that the method appears ill-suited for CM decompositions of large N problems.

4.4   Chapter conclusions

This section has examined the class of linear dipole arrays in the presence of finite conducting ground-planes. While these arrays had few elements compared to the linear ring arrays in Chapter 3, the problems maintained high N values due to the large rectangular ground plate. Operating it as a phased array demonstrated how CM summations are sensitive to breaking electrical symmetry, with broadside excitations achieving higher accuracy with fewer modes. Attempts to further study dips in radiated power were frustrated by
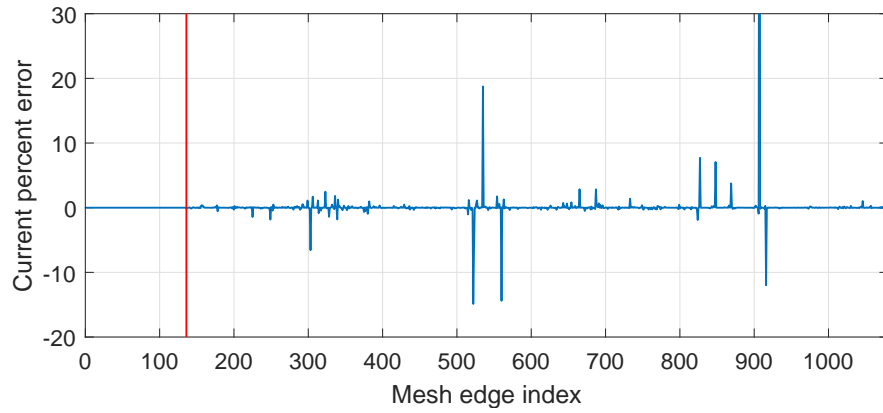
(a) Real current percent error
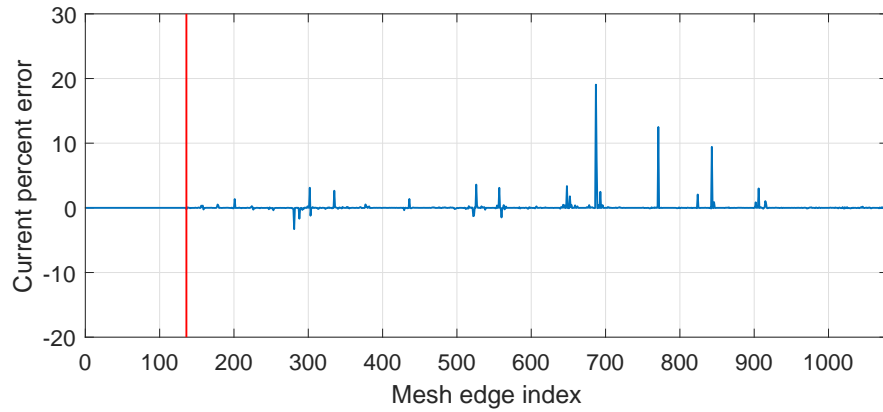
(b) Imaginary current percent error

Figure 4.26: Current percent error as a function of mesh edge index. Values to the left of the vertical red line indicate edges on the array elements. Values to the right of the line indicate edges on the ground-plane.
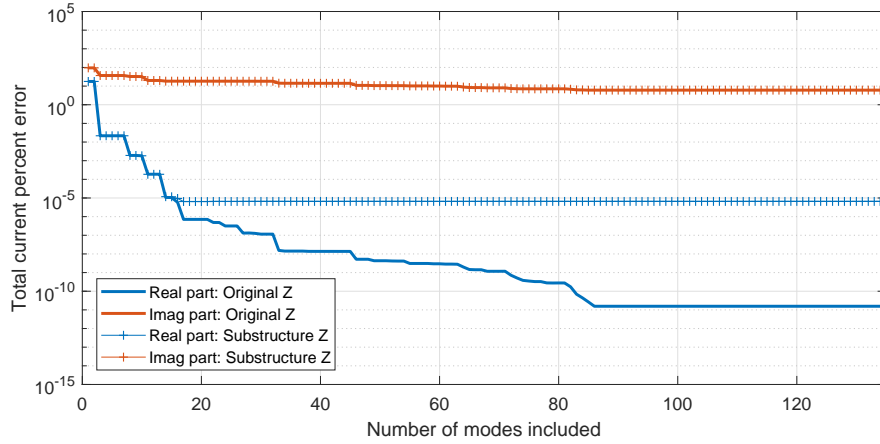
Figure 4.27: Comparison of current percent error values when modes are calculated directly for the entire structure, and when the substructure procedure is used.

the difficulty mode tracking poses for larger problems over appreciable frequency ranges. We demonstrated the differences between ground and array dominant modes and the differing effects they have on the total modal summation accuracy. An eigenvalue based method of differentiating these modes was demonstrated with the use of delta weight values. Finally we examined the application of substructure decomposition to the modal problem and the accuracy penalty it incurs when applied to electrically large problems.

CHAPTER 5

CONCLUSIONS AND FUTURE WORK

This work has investigated the utility and accuracy of using characteristic mode analysis in the study of electrically large finite antenna arrays. Research into characteristic mode analysis has seen a resurgence in recent years and has been implemented in a number of commercial solver suites as well. However, like any computational method it should not be applied blindly and this work illustrates a number of difficulties that can arise when using it on large array problems. We have demonstrated accuracy metrics for single resonant elements, linear arrays, and an array with a finite ground-plane. The metrics are based on eigencurrent and modal far-field projections. The accuracy convergence of modal sums has been shown to vary depending on element symmetry, and whether the structure supports a meaningful imaginary current distribution. These metrics have been utilized to show the sensitivity and behavior of a modal sum applied to a phased array steering a beam away from broadside. Additionally we have demonstrated that popular mode tracking algorithms are still unable to track eigenmodes for our scale of problem across a meaningful range of frequency points. This fact coupled with the computational costs of large N eigenvalue problems calls into question the utility of direct characteristic mode applications to large problems. Attempts to utilize substructure based methods show promise despite the error introduced to ground-plane currents. The presented results are to be used in conjunction with an engineer's knowledge of error tolerance. CM is not a one-size-fits-all approach and this work demonstrates some of the limits of its application.

Utilizing and providing accuracy metrics for alternative modal decompositions is an area of much needed future work. Energy storage and radiation modes [33] show great promise in isolating ground-plane properties from the large radiation problem; however, this method currently is limited to electrically smaller problems. Port focused methods [34, 35] can help reduce

the size of the CM problem for simple antenna elements with known current distributions. Element cell methods may prove to be a more fruitful area of research, where inter-element coupling can be incorporated by iterative perturbation methods, instead of the entire-structure basis approach investigated in this work. We demonstrated the effect of impedance matrix conditioning and the need to relax requirements of purely real modes when the CM problem produces complex results. Further work on studying the impact of these mode definitions is necessary, and can be expanded to array work that includes dielectrics in the modal decomposition [24].

# APPENDIX A

ADDITIONAL MODAL ACCURACY VALUES

Having examined a single-ring element and its CM decomposition we now simulate and study an electric dipole, another common antenna array element. Figure A.1 depicts the total current percent error values for four geometric variations of a $\lambda/2$ dipole, with the impedance matrices computed by FEKO.

An alternative element, a square ring, is tested using FEKO with the results shown in Figure A.2. It was chosen as a test element because of its reduced dimensions of symmetry relative to a circular ring.

Comparing these results with the thin-strip ring results presented in Chapter 3, we can make some observations about the effect of physical symmetry on the modal decomposition of an antenna element, which past works have shown can affect how modes couple to one another [30]. The circular ring has infinitely many axes of symmetry. The square ring has four axes of symmetry. A sufficiently thin strip dipole has one axis of symmetry, assuming it behaves like a thin-wire. We note that square ring does not suffer from the "broken" solutions of the circular ring, where when using the original impedance matrix the error remains high as more modes are added to the summation. The dipole converges most rapidly in terms of real error, achieving near perfect accuracy. Variation 2 of the dipole experiences divergent behavior in the imaginary current summation, a behavior which must be studied further.
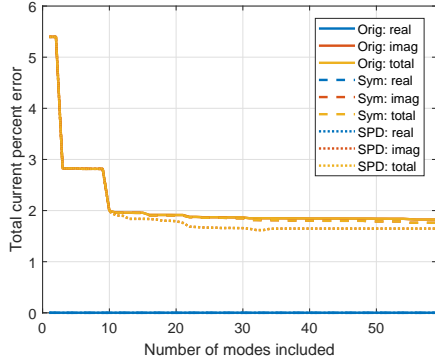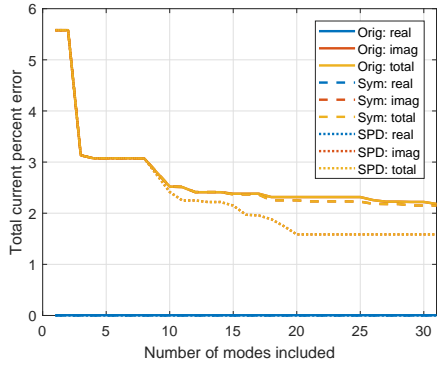
(a) Variation 1:
$w_d = \lambda/100$; $m_l = \lambda/60$
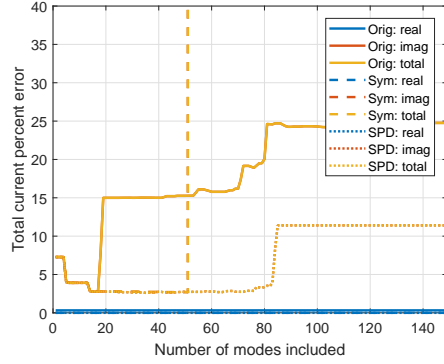
(b) Variation 2:
$w_d = \lambda/50$; $m_l = \lambda/60$
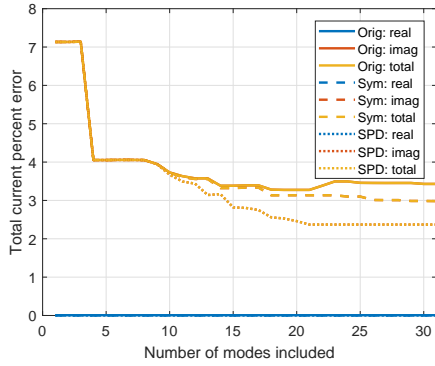
(c) Variation 3:
$w_d = \lambda/50$; $m_l = \lambda/30$

(d) Variation 4:
$w_d = \lambda/100$; $m_l = \lambda/30$

Figure A.1: Total current percent error [Eqs. (3.1) and (3.2)] values for a single thin-strip dipole simulated in FEKO. Four variations were tested, with differing dipole widths (w_d) and maximum mesh segment lengths (m_l), using the original impedance matrix, and two *ex post* conditioned matrices.
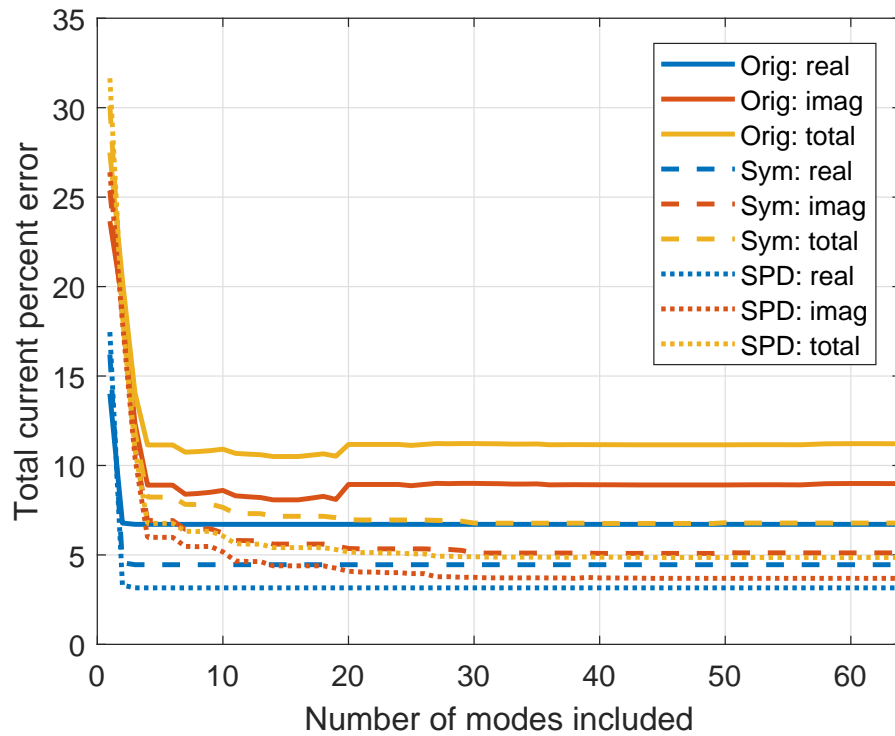
Figure A.2: Total current percent error for a single thin-strip square ring with thin-strip width $w_r = \lambda/100$ and maximum mesh edge lengths $m_l = \lambda/30$, using the original impedance matrix, and two *ex post* conditioned matrices.

APPENDIX B

DELTA MODAL WEIGHT PLOTS

In Section 4.3.2 delta modal weight values are plotted for 1° and 5° beam steering increments. Figures B.1-B.3 present the delta modal weights for 2°, 3°, and 4° increments. The delta weight trends are presented in Table 4.5.
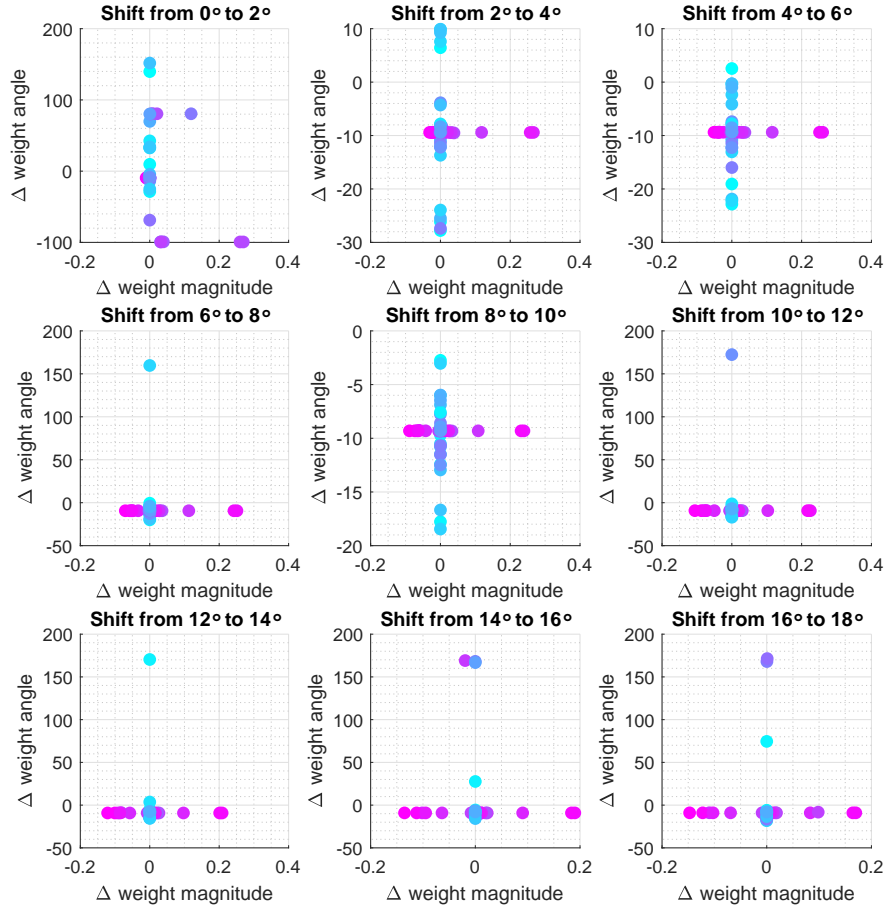
Figure B.1: Delta weight values for a five-element dipole array above a rectangular ground-plane with beam scanned in 2° increments from broadside. The color scale from cyan to magenta indicates the average modal current magnitude at the array ports, ranging from low density (ground-modes) to high density (array-modes).
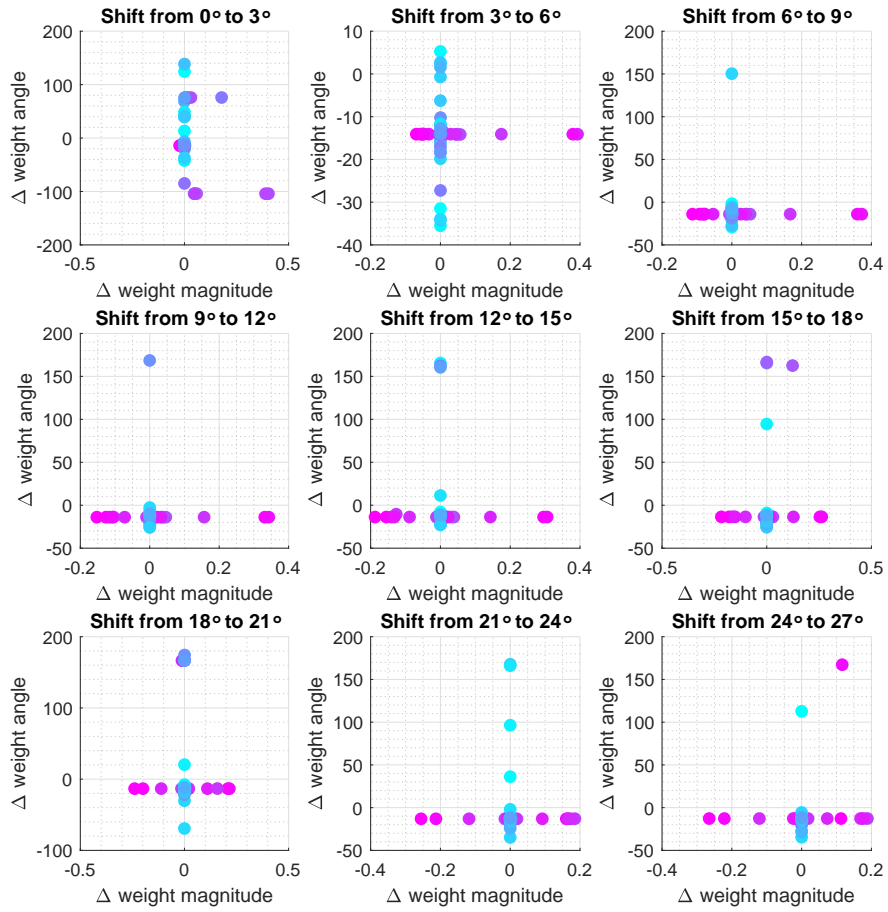
Figure B.2: Delta weight values for a five-element dipole array above a rectangular ground-plane with beam scanned in 3° increments from broadside.
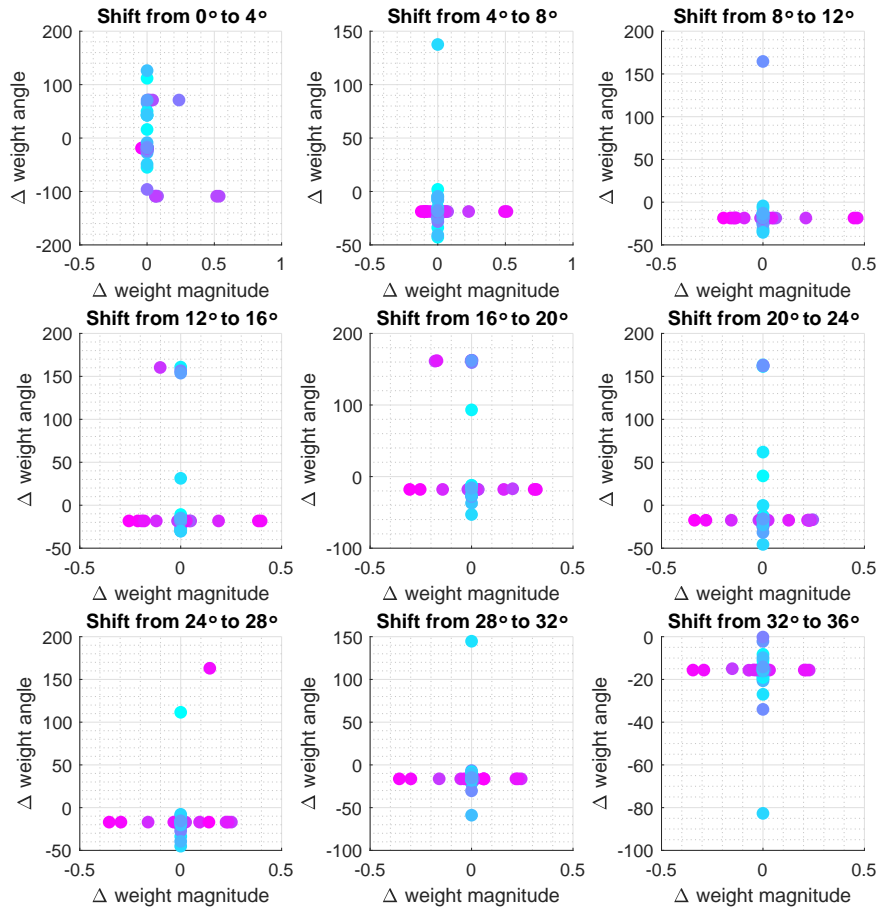
Figure B.3: Delta weight values for a five-element dipole array above a rectangular ground-plane with beam scanned in 4° increments from broadside.

REFERENCES

[1] W. L. Stutzman and G. A. Thiele, *Antenna Theory and Design*. Hoboken, NJ: Wiley, 2013.

[2] B. A. Munk, *Finite Antenna Arrays and FSS*. Wiley-IEEE Press, 2003.

[3] M. Cabedo-Fabrés, E. Antonino-Daviu, A. Valero-Nogueira, and M. Bataller, "The theory of characteristic modes revisited: A contribution to the design of antennas for modern applications," *IEEE Antennas Propag. Mag.*, vol. 49, no. 5, pp. 52–68, Oct. 2007. [Online]. Available: http://ieeexplore.ieee.org/lpdocs/epic03/wrapper.htm?arnumber=4395295 http://ieeexplore.ieee.org/xpls/abs_all.jsp?arnumber=4395295

[4] J. J. Adams and J. T. Bernhard, "A modal approach to tuning and bandwidth enhancement of an electrically small antenna," *IEEE Trans. Antennas Propag.*, vol. 59, no. 4, pp. 1085–1092, Apr. 2011. [Online]. Available: http://ieeexplore.ieee.org/xpls/abs_all.jsp?arnumber=5722973 http://ieeexplore.ieee.org/lpdocs/epic03/wrapper.htm?arnumber=5722973

[5] N. L. Bohannon and J. T. Bernhard, "Design guidelines using characteristic mode theory for improving the bandwidth of PIFAs," *IEEE Trans. Antennas Propag.*, vol. 63, no. 2, pp. 459–465, Feb. 2015. [Online]. Available: http://ieeexplore.ieee.org/lpdocs/epic03/wrapper.htm?arnumber=6965575

[6] Q. Wu, S. Guo, and D. Su, "On the eigenmodes of small conducting objects," *IEEE Antennas Wirel. Propag. Lett.*, vol. 13, pp. 1667–1670, 2014. [Online]. Available: http://ieeexplore.ieee.org/lpdocs/epic03/wrapper.htm?arnumber=6882142

[7] A. J. King, "Characteristic mode theory for closely spaced dipole arrays," Ph.D. dissertation, University of Illinois at Urbana-Champaign, 2015.

[8] T. Lonsky, P. Hazdra, and J. Kracek, "Modal decomposition for arbitrary dipole array," in *2017 Conf. Microw. Tech. Com. 2017*, 2017.

[9] T. Lonsky, P. Hazdra, and J. Kracek, "Design of closely spaced dipole array based on characteristic modes," in *2017 Prog. Electromagn. Res. Symp. - Fall (PIERS - FALL)*, no. 3. IEEE, Nov. 2017. [Online]. Available: http://ieeexplore.ieee.org/document/8293145/ pp. 258–261.

[10] R. J. Garbacz and R. Turpin, "A generalized expansion for radiated and scattered fields," *IEEE Trans. Antennas Propag.*, vol. 19, no. 3, pp. 348–358, May 1971. [Online]. Available: http://ieeexplore.ieee.org/xpls/abs_all.jsp?arnumber=1139935 http://ieeexplore.ieee.org/lpdocs/epic03/wrapper.htm?arnumber=1139935

[11] R. Harrington and J. Mautz, "Theory of characteristic modes for conducting bodies," *IEEE Trans. Antennas Propag.*, vol. 19, no. 5, pp. 622–628, Sep. 1971. [Online]. Available: http://ieeexplore.ieee.org/lpdocs/epic03/wrapper.htm?arnumber=1139999

[12] R. F. Harrington and J. R. Mautz, "Computation of characteristic modes for conducting bodies," *IEEE Trans. Antennas Propag.*, vol. 19, no. 5, pp. 629–639, Sep. 1971.

[13] R. F. Harrington, *Field Computation by Moment Methods*, 1993. [Online]. Available: http://ieeexplore.ieee.org/xpl/bkabstractplus.jsp?bkn=5264934 http://www.amazon.com/Computation-Moment-Methods-Series-Electromagnetic/dp/0780310144

[14] B. Austin and K. Murray, "The application of characteristic-mode techniques to vehicle-mounted NVIS antennas," *IEEE Antennas Propag. Mag.*, vol. 40, no. 1, pp. 7–21, 30, 1998. [Online]. Available: http://ieeexplore.ieee.org/lpdocs/epic03/wrapper.htm?arnumber=667319

[15] B. D. B. Raines and R. G. R. Rojas, "Wideband characteristic mode tracking," *IEEE Trans. Antennas Propag.*, vol. 60, no. 7, pp. 3537–3541, July 2012. [Online]. Available: http://ieeexplore.ieee.org/lpdocs/epic03/wrapper.htm?arnumber=6192307 http://ieeexplore.ieee.org/xpls/abs_all.jsp?arnumber=6192307

[16] D. Bekers, "Finite antenna arrays: An eigencurrent approach," Ph.D. dissertation, Stan Ackermans Institute of the Technische Universiteit Eindhoven, 2004.

[17] D. J. Bekers, S. J. Van Eijndhoven, A. A. Van De Ven, P. P. Borsboom, and A. G. Tijhuis, "Eigencurrent analysis of resonant behavior in finite antenna arrays," *IEEE Trans. Microw. Theory Tech.*, vol. 54, no. 6, pp. 2821–2829, 2006.

[18] D. Bekers, S. van Eijndhoven, and A. Tijhuis, "An eigencurrent approach for the analysis of finite antenna arrays," *IEEE Trans. Antennas Propag.*, vol. 57, no. 12, pp. 3772–3782, Dec. 2009. [Online]. Available: http://ieeexplore.ieee.org/lpdocs/epic03/wrapper.htm?arnumber=5165016

[19] M. Capek, V. Losenicky, L. Jelinek, and M. Gustafsson, "Validating the characteristic modes solvers," *IEEE Trans. Antennas Propag.*, vol. 65, no. 8, pp. 4134–4145, 2017.

[20] E. Wilken-Resman, "GPU-Accelerated MoM Toolkit," 2018.

[21] W. Gibson, *The Method of Moments in Electromagnetics.* Chapman & Hall/CRC, 2008.

[22] J.-M. Jin, *Theory and Computation of Electromagnetic Fields.* Wiley, 2015.

[23] S. Rao, D. Wilton, and A. Glisson, "Electromagnetic scattering by surfaces of arbitrary shape," *IEEE Trans. Antennas Propag.*, vol. 30, no. 3, pp. 409–418, May 1982. [Online]. Available: http://ieeexplore.ieee.org/lpdocs/epic03/wrapper.htm?arnumber=1142818

[24] L. Guan, Z. He, D. Ding, and R. Chen, "Efficient characteristic mode analysis for radiation problems of antenna arrays," *IEEE Trans. Antennas Propag.*, vol. 67, no. 1, pp. 1–1, 2018. [Online]. Available: https://ieeexplore.ieee.org/document/8496873/

[25] M. Cabedo-Fabrés, E. Antonino-Daviu, D. Escuderos, and V. Rodrigo-Penarrocha, "On the application of characteristic modes for the analysis of large scale antenna problems," *IET Semin. Dig.*, pp. 623–623, 2007. [Online]. Available: http://link.aip.org/link/IEESEM/v2007/i11961/p623/s1&Agg=doi

[26] R. F. Harrington, J. R. Mautz, and Y. Chang, "Characteristic modes for dieletric and magnetic bodies," *IEEE Trans. Antennas Propag.*, vol. 20, no. 2, pp. 194–198, 1972.

[27] D. Tayli, M. Capek, L. Akrou, V. Losenicky, L. Jelinek, and M. Gustafsson, "Accurate and efficient evaluation of characteristic modes," *IEEE Trans. Antennas Propag.*, vol. 66, no. 12, pp. 7066–7075, 2018.

[28] M. Gustafsson, "EM modes for model order reduction and antenna optimization," in *IEEE Antennas Propag. Soc. AP-S Int. Symp. APS2018*, no. 6, 2018.

[29] M. T. Ma, *Theory and Application of Antenna Arrays.* Wiley, 1974.

[30] K. R. Schab, J. M. Outwater, M. W. Young, and J. T. Bernhard, "Eigenvalue crossing avoidance in characteristic modes," *IEEE Trans. Antennas Propag.*, pp. 1–1, 2016. [Online]. Available: http://ieeexplore.ieee.org/lpdocs/epic03/wrapper.htm?arnumber=7446294

[31] Z. Miers and B. K. Lau, "Wideband characteristic mode tracking utilizing far-field patterns," *IEEE Antennas Wirel. Propag. Lett.*, vol. 14, pp. 1658–1661, 2015. [Online]. Available: http://ieeexplore.ieee.org/lpdocs/epic03/wrapper.htm?arnumber=7069193

[32] J. Ethier and D. McNamara, "Sub-structure characteristic mode concept for antenna shape synthesis," *Electron. Lett.*, vol. 48, no. 9, p. 471, 2012. [Online]. Available: http://digital-library.theiet.org/content/journals/10.1049/el.2012.0392

[33] K. R. Schab and J. T. Bernhard, "Radiation and energy storage current modes on conducting structures," *IEEE Trans. Antennas Propag.*, vol. 63, no. 12, pp. 5601–5611, 2015.

[34] P. Hazdra, T. Lonsky, and J. Kracek, "Modal decomposition theory for arrays of dipoles," in *2017 11th Eur. Conf. Antennas Propag.* IEEE, Mar. 2017. [Online]. Available: http://ieeexplore.ieee.org/document/7928351/ pp. 2660–2662.

[35] P. Hazdra, T. Lonsky, and J. Kracek, "Characteristic modes of dipole arrays," *IEEE Antennas Wirel. Propag. Lett.*, vol. 17, no. 6, pp. 998–1001, 2018.